

# The temperature of the diffuse H I in the Milky Way II: Gaussian decomposition of the H I 21cm absorption spectra

Nirupam Roy<sup>1\*</sup>, Nissim Kanekar<sup>2\*</sup> and Jayaram N. Chengalur<sup>2\*</sup>

<sup>1</sup>Max-Planck-Institut für Radioastronomie, Auf dem Hügel 69, D-53121, Bonn, Germany

<sup>2</sup>National Centre for Radio Astrophysics, TIFR, Post Bag 3, Ganeshkhind, Pune 411 007, India

Accepted yyyy month dd. Received yyyy month dd; in original form yyyy month dd

## ABSTRACT

We discuss physical conditions in Galactic neutral hydrogen based on deep, high velocity resolution interferometric H I 21cm absorption spectroscopy towards 33 compact extra-galactic radio sources. The H I 21cm optical depth spectra have root-mean-square noise values  $\lesssim 10^{-3}$  per  $1 \text{ km s}^{-1}$  velocity channel, i.e., sufficiently sensitive to detect H I 21cm absorption by the warm neutral medium (WNM). Comparing these spectra with H I 21cm emission spectra from the Leiden-Argentine-Bonn (LAB) survey, we show that some of the absorption detected on most sightlines must arise in gas with temperatures higher than that in the stable cold neutral medium (CNM). A multi-Gaussian decomposition of 30 of the H I 21cm absorption spectra yielded very few components with line widths in the temperature range of stable WNM, with no such WNM components detected for sixteen of the thirty sightlines. We find that some of the detected H I 21cm absorption along thirteen of these sightlines must arise in gas with spin temperatures larger than the CNM range. For these sightlines, we use very conservative estimates of the CNM spin temperature and the non-thermal broadening to derive strict upper limits to the gas column densities in the CNM and WNM phases. Comparing these upper limits to the total H I column density, we find that typically at least 28% of the gas must have temperatures in the thermally unstable range (200 – 5000 K). Our observations hence robustly indicate that a significant fraction of the gas in the Galactic interstellar medium has temperatures outside the ranges expected for thermally stable gas in two-phase models.

**Key words:** ISM: atoms – ISM: general – ISM: kinematics and dynamics – ISM: structures – radio lines: ISM

## 1 INTRODUCTION

In the thermal steady-state model for neutral hydrogen (H I) in the Galactic interstellar medium (ISM), two distinct stable phases co-exist in pressure equilibrium (e.g. Field 1965; Field et al. 1969; Wolfire et al. 1995, 2003). These are (1) a cold phase (the cold neutral medium, CNM), with high density ( $n \approx 10 - 100 \text{ cm}^{-3}$ ) and a high H I-21 cm optical depth that gives rise to the narrow absorption features seen towards continuum radio sources, and (2) a warm diffuse phase (the warm neutral medium, WNM) with low density ( $n \approx 0.1 - 1 \text{ cm}^{-3}$ ), which contributes to the H I emission, but is extremely difficult to detect in absorption due to its low optical depth. The models (e.g. Wolfire et al. 1995) find that gas in the stable CNM phase would have kinetic temperatures  $T_k \sim 40 - 200 \text{ K}$ , while gas in the stable WNM phase would have kinetic temperatures of  $T_k \sim 5000 - 8000 \text{ K}$ . Over the last few decades, a number of H I-21 cm studies have established that the ISM indeed contains cold atomic gas in the temperature

range  $\sim 40 - 200 \text{ K}$ , consistent with theoretical expectations (e.g. Clark et al. 1962; Radhakrishnan et al. 1972; Dickey et al. 1978; Heiles & Troland 2003a; Roy et al. 2006). However, observational estimates of WNM temperature are quite rare (Heiles & Troland 2003b; Kanekar et al. 2003) and very little is as yet known about physical conditions in the WNM.

In the two-phase models, H I at intermediate temperatures is unstable and such gas is expected to quickly evolve into one of the stable phases. Gas at intermediate temperatures is thus expected to exist “only as a transient phenomenon” (Field et al. 1969). The thermal timescale derived from the heating or cooling rates is  $\sim 2 \times 10^4 \text{ yr}$  for the CNM, and about 100 times larger for the WNM (Wolfire et al. 1995). On the other hand, the timescale between physical disturbances in the ISM (i.e. the typical time interval between significant pressure fluctuations) due to the propagation of supernova shocks is  $\approx 4 \times 10^5 \text{ yr}$  (McKee & Ostriker 1977; Wolfire et al. 1995). Thus, while the CNM can be assumed to be in the thermal steady state, equilibrium conditions may not prevail in the WNM. However, Wolfire et al. (1995) argue that physical conditions in the WNM will evolve towards the steady state, and the

\* E-mail: nirupam@mpifr-bonn.mpg.de (NR); nkanekar@ncra.tifr.res.in (NK); chengalu@ncra.tifr.res.in (JNC)

steady state conditions could be thought to “represent an average of the conditions to be expected in the actual WNM”.

Recently, there have been suggestions, based both on H I 21 cm observations and simulations, that a significant fraction of the Galactic H I may have kinetic temperatures in the unstable range, 500 – 5000 K (Heiles & Troland 2003a; Heiles & Troland 2003b; Kanekar et al. 2003). Numerical simulations of the ISM suggest that dynamical processes like turbulence may drive H I from the stable CNM or WNM phases to the thermally unstable phase (e.g. Audit & Hennebelle 2005; Saury et al. 2013). This could result in significant amounts of unstable neutral gas, unlike the case of the standard two-phase models. Observational evidence for the presence of unstable gas stems from the work of Heiles & Troland (2003a), who carried out high velocity resolution H I 21 cm absorption and emission studies towards 79 compact radio sources with the Arecibo telescope. They then modelled the H I 21 cm absorption and emission spectra as the sum of thermally-broadened Gaussian components to estimate the kinetic temperature and fraction of gas in the different temperature phases. The unstable phase was found to make up nearly 50% of the H I along their sightlines (Heiles & Troland 2003b). However, the single-dish spectra used in their analysis are subject to large systematic effects, both due to contamination from stray radiation coming through the large sidelobes of the Arecibo telescope and the fact that single-dish H I 21 cm absorption spectra must be corrected for the H I emission in the beam. The sidelobe contamination in the emission spectra is especially important here, because the results pertaining to gas in the unstable phase were based on the fits to the emission spectra.

Conversely, Kanekar et al. (2003) carried out high velocity resolution *interferometric* H I 21 cm absorption studies along two sightlines using the Australia Telescope Compact Array (ATCA), with multi-Gaussian fits to the absorption spectra alone [see also Lane et al. (2000) and Kanekar et al. (2001) for a similar approach in damped Lyman- $\alpha$  systems]. Kanekar et al. (2003) found that a significant fraction of gas is in the thermally unstable phase; however the sample was small, with only two lines of sight. Such deep interferometric observations allow the possibility of obtaining an “clean” determination of the H I 21 cm absorption profile, by resolving out the H I 21 cm emission, and thus, of directly detecting the WNM in absorption. We have recently begun a large observational program to probe neutral atomic gas in the ISM through interferometric H I 21 cm absorption studies with the Westerbork Synthesis Radio Telescope (WSRT) and the Giant Metrewave Radio Telescope (GMRT), following the approach of Kanekar et al. (2003). The observations, data analysis, spectra and integrated properties for each of the 34 observed sightlines were presented by Roy et al. (2013, hereafter, Paper I). In this paper, we describe the multi-Gaussian parametrisation of the 33 absorption spectra with detected H I 21 cm absorption, including the two ATCA targets of Kanekar et al. (2003), and their implications for physical conditions in the interstellar medium.

## 2 SPIN, KINETIC AND DOPPLER TEMPERATURES IN THE ISM

In Paper I, we discussed in detail the spin temperature  $T_s$  and the kinetic temperature  $T_k$ , the two main temperatures used to characterize the neutral atomic phases of the interstellar medium. We will not repeat this discussion here, but will simply assume that  $T_s \approx T_k$  for the CNM and that  $T_s \lesssim T_k$  in the other temperature phases, with  $T_s \leq 5000$  K (e.g. Liszt 2001). The spin temperature along a

sightline is estimated from the ratio of the total H I column density to the velocity-integrated H I 21 cm optical depth. The H I column density can be estimated either from the H I 21 cm emission spectrum along a neighbouring sightline (e.g. Heiles & Troland 2003a) or from an absorption spectrum in the damped Lyman- $\alpha$  line (e.g. Wakker et al. 2011), while the H I 21 cm optical depth is, of course, measured from H I 21 cm absorption studies towards a background radio source. For an arbitrary sightline, the spin temperature obtained from the above procedure is the column density weighted harmonic mean of the spin temperatures of individual “clouds” along the sightline, and does not provide direct information on the gas temperature. For large H I 21 cm optical depths, there are further complications because one does not *a priori* know the distribution of clouds along the sightline, making it difficult to correct for self-absorption in the H I 21 cm emission spectrum while estimating the total H I column density. Attempts to fit for this distribution along the line of sight have so far not been successful (e.g. Heiles & Troland 2003a). A variation of the above procedure is to decompose the absorption and emission spectra into Gaussian components and then determine the spin temperature of individual components (e.g. Dickey et al. 1978; Payne et al. 1982; Heiles & Troland 2003a). This has so far only been successful for the cold phase, due to the high spectral dynamic range required to detect the WNM in absorption. Even here, there are complications because one is measuring the emission profile along a different line of sight (and generally a larger field of view) than that for the absorption profile, and small scale variations in the H I distribution could invalidate the analysis.

The kinetic temperature  $T_k$  is the temperature that characterizes the velocity distribution of the H I atoms on small scales (i.e. scales on which bulk motions are negligible). Because these scales are generally inaccessible to observations, the gas kinetic temperature is instead typically estimated from the “doppler temperature” ( $T_D$ ), which is derived from the full-width-at-half-maximum (FWHM) of an H I 21 cm component by the relation  $T_D = 21.855 \times \Delta V^2$  K, where  $\Delta V$  is the FWHM in  $\text{km s}^{-1}$ . If the line width is dominated by thermal broadening, with negligible contributions from turbulence, bulk motions, etc, one would have  $T_k = T_D$ . However, in general,

$$T_D = T_k + \frac{m_H v_{\text{turb}}^2}{k_B}, \quad (1)$$

where  $v_{\text{turb}}$  gives the contribution to the line width from non-thermal motions,  $m_H$  is the mass of the hydrogen atom and  $k_B$  is the Boltzmann constant. If such non-thermal broadening is negligible, one can use  $T_D$  and  $T_k$  interchangeably. In the general case, the doppler temperature only provides an upper limit to the kinetic temperature.

To summarize, in H I 21 cm absorption spectra, both the spin and doppler temperatures affect the line profile; the spin temperature determines the total integrated optical depth, while the doppler temperature (i.e. the combination of the kinetic temperature and any non-thermal motions) determines the line width. If one assumes that non-thermal contributions to the line widths are small (e.g. Heiles & Troland 2003a), one can estimate the kinetic temperature from the line profile.

The main differences between the present work and the analysis of Heiles & Troland (2003a) is that (i) we obtain our H I 21 cm absorption spectra from high angular resolution interferometric observations, unaffected by the H I 21 cm emission, (ii) we carry out the multi-Gaussian decomposition for the H I 21 cm absorption profiles only, and (iii) we use these decompositions to

identify lines of sight along which there appears to be very little of the classical WNM, but the conclusions that we draw about the fractions of CNM and WNM are independent of the assumption that the doppler temperature approximates the kinetic temperature.

### 3 THE SAMPLE

We have used the Very Large Array (VLA) calibrator list<sup>1</sup> to select a sample of bright, compact extra-galactic background radio sources for use as targets for deep H I-21 cm absorption spectroscopy to probe physical conditions in the intervening Galactic neutral hydrogen. 32 such compact sources (all with 1.4 GHz flux densities  $> 3.5$  Jy) were observed with the Westerbork Synthesis Radio Telescope (WSRT) and the Giant Metrewave Radio Telescope (GMRT) between 2005 and 2008; the observations, data analysis and spectra are described in detail in Paper I. The velocity resolutions of the spectra were  $\approx 0.41$  km s<sup>-1</sup> (GMRT) and  $\approx 0.26$  km s<sup>-1</sup> (WSRT), except for two WSRT targets, B1328+254 and B1328+307, which had a resolution of  $\approx 0.52$  km s<sup>-1</sup>. The observations were designed to detect the warm neutral medium in absorption, even for low H I column densities,  $\geq 2 \times 10^{20}$  cm<sup>-2</sup>, and high spin temperatures  $T_s \approx 5000$  K. The root-mean-square (RMS) optical depth noise on the spectra was  $\lesssim 10^{-3}$  at a resolution of 1 km s<sup>-1</sup>. H I-21 cm absorption was detected along 31 sightlines, with only a single non-detection, towards B0438–436 (Paper I).

In addition, two similar bright, compact sources were observed by Kanekar et al. (2003) with the ATCA, with a velocity resolution of  $\approx 0.41$  km s<sup>-1</sup> and an RMS optical depth noise of  $\approx 10^{-3}$  per 0.41 km s<sup>-1</sup>. We include these two sources with the 31 sources of Paper I with detected H I-21 cm absorption in the following analysis. The full sample considered in this paper thus consists of 33 compact sources with high velocity resolution ( $\approx 0.26 - 0.52$  km s<sup>-1</sup>) interferometric H I-21 cm absorption spectra of RMS optical depth  $\lesssim 10^{-3}$  per 1 km s<sup>-1</sup> velocity channel. We have also obtained H I-21 cm emission spectra along neighbouring sightlines from the Leiden-Argentine-Bonn survey (Kalberla et al. 2005; Bajaja et al. 2005), at a velocity resolution of  $\approx 1.03$  km s<sup>-1</sup>.

The integrated properties along all sightlines of the sample are presented in Paper I (see also Kanekar et al. 2011). For completeness, a few of these properties are summarized here in Table 1: the columns of this table contain (1) the source name (using the B1950 convention), (2) the total H I column density along the sightline,  $N(\text{H I})$ , using the isothermal estimate (Chengalur et al. 2013), (3) the integrated H I-21 cm optical depth,  $\int \tau dV$ , in km s<sup>-1</sup>, and (4) the velocity extent containing 90% of the H I-21 cm emission,  $\Delta V_{90}$ , in km s<sup>-1</sup>.

As shown in Chengalur et al. (2013), the isothermal estimate, in general, provides a significantly more accurate estimate of the total H I column density than the usually used optically-thin estimate. We also emphasize that (despite the name) the isothermal estimate does not assume that all of the gas in the Galaxy is at a single temperature, but rather that it uses the total optical depth and brightness temperature measured along the line of sight to find the temperature that leads to the best estimate of the total H I column density. The simulations in Chengalur et al. (2013) show that this estimate works well even at very large optical depths as well as in situations where the temperature varies significantly along the line

**Table 1.** The full sample of 34 sources

Source	$N(\text{H I})$ $\times 10^{20}$ cm <sup>-2</sup>	$\int \tau dV$ km s <sup>-1</sup>	$\Delta V_{90}$ km s <sup>-1</sup>
B0023-263	1.623 ± 0.013	0.0254 ± 0.0050	101
B0114-211	1.421 ± 0.019	0.1354 ± 0.0054	61
B0117-155	1.452 ± 0.017	0.0307 ± 0.0042	36
B0134+329	4.330 ± 0.019	0.443 ± 0.002	43
B0202+149	4.803 ± 0.016	0.7472 ± 0.0047	24
B0237-233	2.132 ± 0.020	0.2938 ± 0.0040	32
B0316+162	10.09 ± 0.62	2.964 ± 0.004	24
B0316+413	13.64 ± 0.51	1.941 ± 0.003	49
B0355+508	115 ± 43	45.8 ± 1.1	59
B0404+768	11.06 ± 0.42	1.945 ± 0.005	124
B0407-658	3.408 ± 0.030	0.5481 ± 0.0070	64
B0429+415	41.3 ± 1.6	10.879 ± 0.007	66
B0438-436	1.319 ± 0.012	< 0.02	63
B0518+165	23.6 ± 5.4	6.241 ± 0.007	43
B0531+194	28.8 ± 1.5	4.062 ± 0.005	32
B0538+498	21.31 ± 0.94	5.618 ± 0.003	71
B0831+557	4.499 ± 0.020	0.483 ± 0.005	75
B0834-196	6.86 ± 0.21	0.973 ± 0.005	68
B0906+430	1.283 ± 0.020	0.0512 ± 0.0030	99
B1151-348	7.06 ± 0.12	0.714 ± 0.004	125
B1245-197	3.711 ± 0.017	0.158 ± 0.005	55
B1328+254	1.108 ± 0.019	0.0214 ± 0.0031	67
B1328+307	1.221 ± 0.016	0.0717 ± 0.0018	54
B1345+125	1.920 ± 0.011	0.305 ± 0.005	34
B1611+343	1.360 ± 0.019	0.0187 ± 0.0027	66
B1641+399	1.078 ± 0.018	0.0088 ± 0.0024	75
B1814-637	6.66 ± 0.27	0.9974 ± 0.0067	39
B1827-360	8.13 ± 0.40	1.542 ± 0.003	58
B1921-293	7.44 ± 0.41	1.446 ± 0.006	53
B2050+364	28.53 ± 0.96	3.024 ± 0.010	87
B2200+420	18.59 ± 0.98	3.567 ± 0.016	91
B2203-188	2.381 ± 0.011	0.2483 ± 0.0042	48
B2223-052	4.61 ± 0.22	1.034 ± 0.003	23
B2348+643	88 ± 16	32.517 ± 0.031	103

of sight. We note also that for the lines of sight that we consider here, the difference between the isothermal estimate and the optically thin estimate is  $< 30\%$  (see Table 2 of Roy et al. 2013). Our conclusions would remain essentially unchanged were we to use the optically-thin estimate instead of the isothermal one.

### 4 CAN ALL THE DETECTED H I-21 cm ABSORPTION ORIGINATE IN THE CNM ?

One of the standard tenets of the ISM literature is that the warm neutral medium contributes to the H I-21 cm emission but is not detectable in H I-21 cm absorption due to its low optical depth (e.g. Kulkarni & Heiles 1988). Wide absorption components are hence generally assumed to arise from non-thermally broadened CNM. For example, this is the model used by Heiles & Troland (2003a) to model their H I-21 cm absorption/emission spectra. Since our survey was designed to have sufficient sensitivity to detect absorption from the WNM, the first question that one would like to address is: do our absorption spectra in fact definitely contain absorption from gas which is not in the CNM phase, or can all the absorption be accounted for by the CNM?

In order to address this issue, we consider a strawman model

<sup>1</sup> A description of the VLA calibrator list can be obtained at <https://science.nrao.edu/facilities/vla/docs/manuals/cal>.

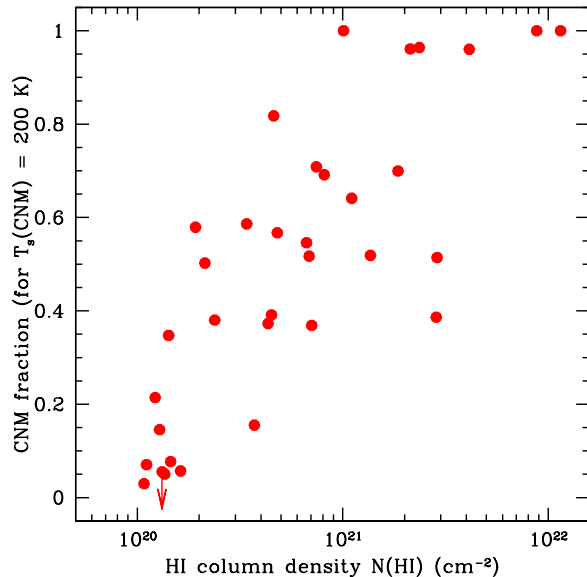


**Figure 1.** The maximum CNM fraction along each sightline, assuming a CNM spin temperature of 200 K, plotted as a function of total H I column density. See Section 4 for details.

in which all the H I-21 cm absorption arises in the CNM, at kinetic temperatures 40 – 200 K (and  $T_s = T_k$ ). The CNM column density along each sightline is then given by

$$N(\text{CNM}) = 1.823 \times 10^{18} \times T_{s,\text{CNM}} \times \int \tau dV, \quad (2)$$

where  $T_{s,\text{CNM}}$  is the harmonic mean spin temperature of the CNM along the sightline. Since the CNM spin temperature range is 40 – 200 K, the harmonic mean CNM spin temperature must lie within this range, with a maximum possible value of 200 K. Thus, an upper limit to the CNM column density for each sightline can be obtained by assuming  $T_{s,\text{CNM}} = 200$  K in equation 2, and using the values for  $\int \tau dV$  from column (3) of Table 1. The ratio of this upper limit to the total H I column density listed in column (2) of the table then gives an upper limit to the CNM fraction along the sightline. Fig. 1 plots this upper limit to the CNM fraction on each sightline, i.e. the ratio  $N(\text{CNM})/N(\text{H I})$ , against the total H I column density  $N(\text{H I})$ . We obtain a median CNM fraction of  $\sim 0.52$  in the sample of 34 sources, with values ranging from  $< 0.055$  to 1. It should be emphasized that these are *upper* limits to the CNM fraction, because we have assumed that (i) all the observed absorption arises from the CNM and (ii) the CNM has a harmonic mean spin temperature of 200 K, the highest value in the CNM range.

Next, for each sightline, the difference  $[N(\text{H I}) - N(\text{CNM})]$  then gives the amount of “residual” H I with  $T_k > 200$  K along each sightline. Note that, in our strawman model, this gas is *not detected in absorption*. We can thus immediately test the veracity of the model by checking whether the sensitivity in the individual spectra is sufficient to detect this residual gas in absorption. For this purpose, we assume a worst-case scenario, wherein the residual gas has  $T_s = 5000$  K and line FWHM equal to  $\Delta V_{90}$  of the emission profile. These are extremely conservative assumptions, as both the high spin temperature and the large line FWHM reduce the peak H I-21 cm optical depth, making it more difficult to detect a given H I column density in absorption. With these assumptions, we compute  $\Delta N(\text{H I})$ , the  $1\sigma$  sensitivity of each spectrum to H I-

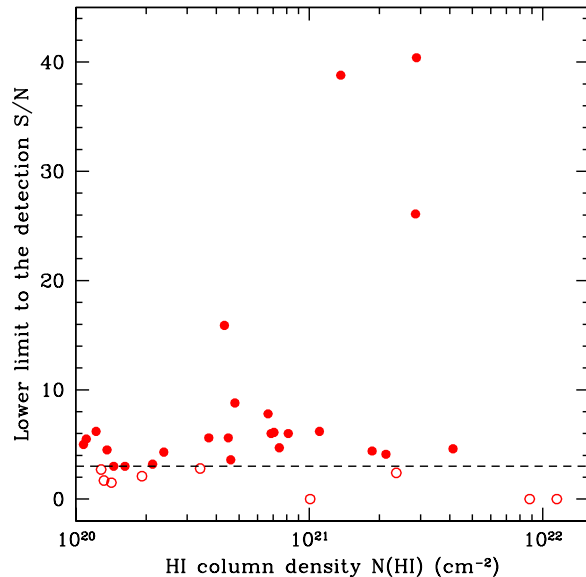


**Figure 2.** The S/N at which “residual” gas with  $T_s = 5000$  K and line FWHM =  $\Delta V_{90}$  (of the LAB emission spectra) would have been detected in the H I-21 cm absorption spectra of our sample; the dashed horizontal line indicates a detection of  $3\sigma$  significance. This assumes a simple model in which all of the detected H I-21 cm absorption arises from the CNM, with  $T_s = 200$  K, while the emission arises in both CNM and WNM. The figure shows that H I-21 cm absorption from the residual gas would have been detected at high significance along 25 of the 34 sightlines of the full sample of Paper I, even for very conservative assumptions. See Section 4 for details.

21 cm absorption from gas with the above line FWHM and spin temperature.

The results of this analysis are summarized in Fig. 2, which plots the signal-to-noise ratio (S/N) at which absorption from the residual gas would have been detected in our H I-21 cm absorption spectra versus the H I column density; the dashed horizontal line indicates a  $3\sigma$  detection. There are three sightlines (towards B0355+508 and B2348+643, the two sources with the lowest Galactic latitudes, and B0316+362) where the (S/N) is listed as zero, as the derived CNM column density is larger than the total H I column density. For these sightlines, the average CNM spin temperature must be lower than the assumed 200 K, and one cannot rule out the possibility that all the H I-21 cm absorption arises in the CNM (or, indeed, that all the H I along the sightline is in the CNM!). However, in 25 of the 34 cases, the spectra are sufficiently sensitive to detect H I-21 cm absorption from the residual gas (at  $\geq 3\sigma$  significance), even for our very conservative assumptions. We emphasize that gas at lower spin temperatures ( $T_s < 5000$  K) or with line FWHMs lower than  $\Delta V_{90}$  (as would be typical) would have been detected at even higher significance. We thus find that a strawman model in which all the absorption arises from the CNM is clearly ruled out: *most of our H I-21 cm absorption spectra must contain absorption from gas with  $T_s \gg 200$  K*. We will return to the issue of the actual temperature of the absorbing gas in Sec. 6.4.

## 5 THE GAUSSIAN PARAMETRISATION

The simplest way of modelling an absorption profile is to treat it as arising from a number of absorbing “clouds” along the line

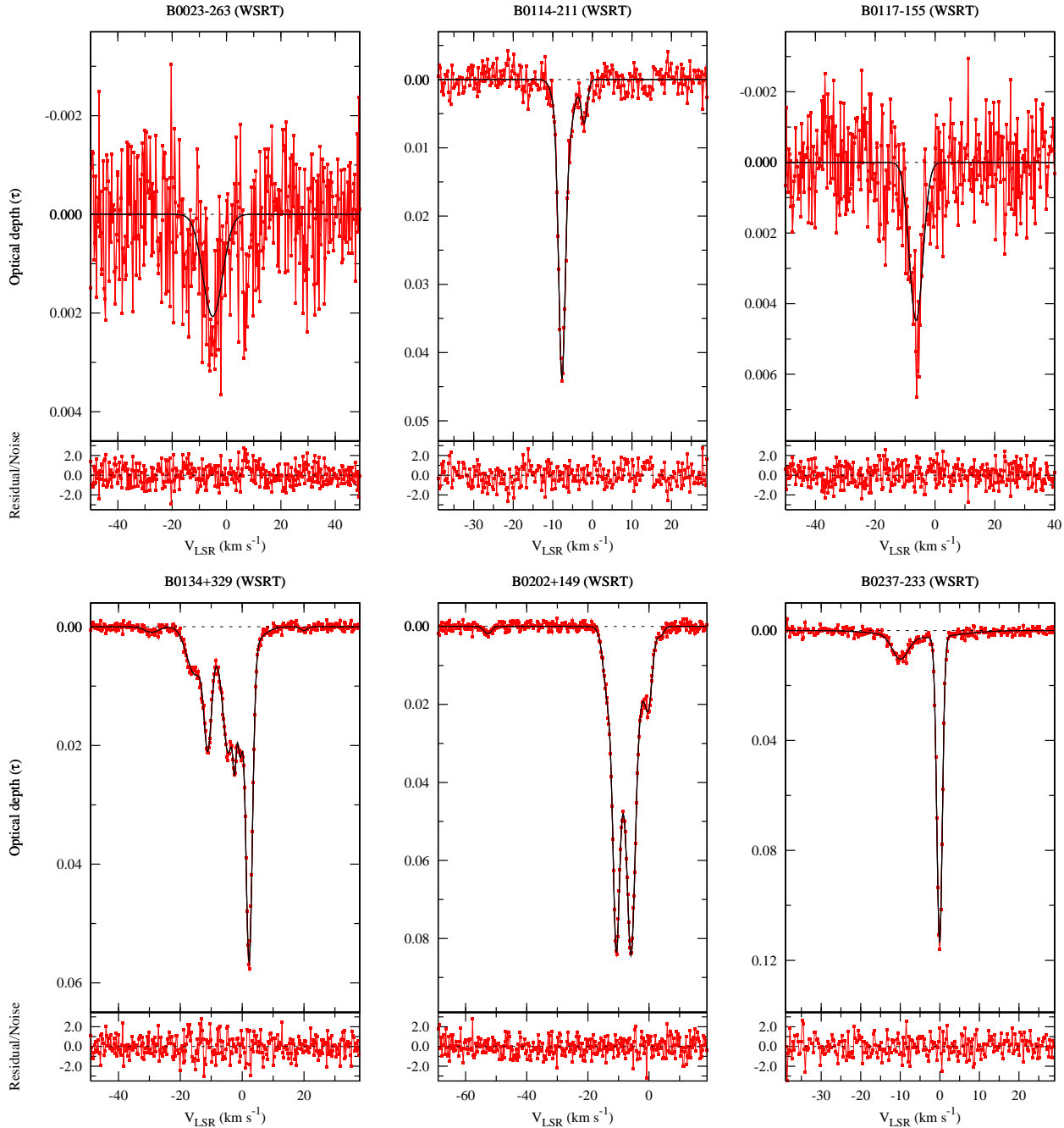


**Figure 3.** H I-21 cm absorption spectra and multi-Gaussian fits for the 30 sources of the sample, ordered by right ascension. The source name and the telescope used to obtain the spectrum is listed above each figure. For each source, the upper panel contains the multi-Gaussian fit overlaid on the H I-21 cm optical depth profile, while the lower panel shows the fit residuals (normalized by the RMS optical depth noise). In most cases, the full velocity range covered by the absorption spectrum is not shown, to make it easier to view the profile.

of sight. If each cloud is individually in equilibrium, at a kinetic temperature  $T_k$ , its line profile would be a “Voigt” profile, a convolution of a Gaussian function with a Lorentzian, which reduces to a Gaussian for unsaturated absorption lines. As such, the simplest physically-motivated model for an unsaturated absorption profile consists of a sum of multiple Gaussian components, with the width of each component determined by the kinetic temperature of the gas. In principle, such a Gaussian decomposition allows one to derive the kinetic temperature of individual “clouds”. Modelling absorption spectra as a superposi-

tion of Gaussian components has hence long been popular in H I-21 cm absorption studies (e.g. Mebold 1972; Radhakrishnan et al. 1972; Mebold et al. 1982; Lane et al. 2000; Kanekar et al. 2001; Heiles & Troland 2003a; Heiles & Troland 2003b; Kanekar et al. 2003). Indeed, the results of Heiles & Troland (2003a) that a significant fraction of the WNM is in the unstable phase are critically dependent on the use of such a multi-Gaussian model for the H I-21 cm emission and absorption spectra *and* the assumption that the line widths predominantly arise from thermal motions.

Unfortunately, it has also long been appreciated that the above

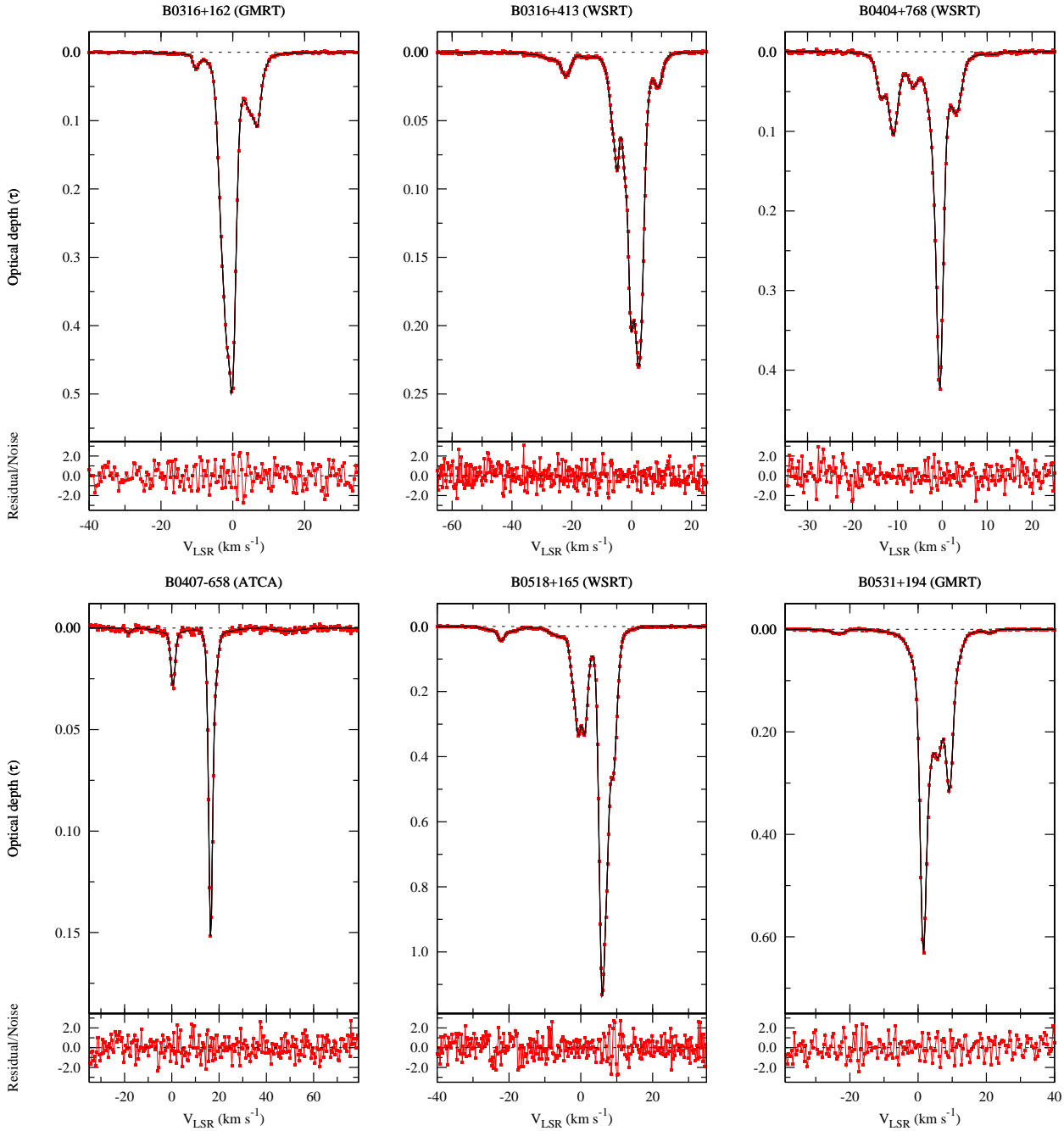


**Figure 3.** (contd.) H I 21 cm absorption spectra and multi-Gaussian fits for the 30 sources of the sample.

interpretation is not necessarily physically meaningful (e.g. Mebold 1972). For example, it is not at all obvious that the individual Gaussian components correspond to distinct physical entities, i.e. whether a typical sightline consists of multiple clouds in internal equilibrium. Non-thermal motions are well known in galaxies, and could lead to distortions of the absorption profile from a Gaussian shape. Even in the case of turbulent broadening, which also yields a Gaussian profile, the final line width is determined by a combination of the kinetic temperature and the turbulent motions, and hence only yields an upper limit to the kinetic temperature. Finally, Gaussian functions do not form an orthogonal basis, implying that

a decomposition is formally not unique, especially in the presence of noise.

Attempts have also been made to model line profiles by assuming a specific form for the density and/or temperature distribution in H I clouds and local isobaricity (e.g. Braun & Kanekar 2005). Note that theoretical models of the ISM are based on local isobaricity, as assumed in the above model, and do not require that individual clouds be isothermal. Conversely, the Gaussian decomposition is strictly valid for cases where each “cloud” along the sightline is isothermal. However, while it is certainly possible to model spectral lines along the lines of Braun & Kanekar (2005), there has so far been no obvious physical motivation for a specific

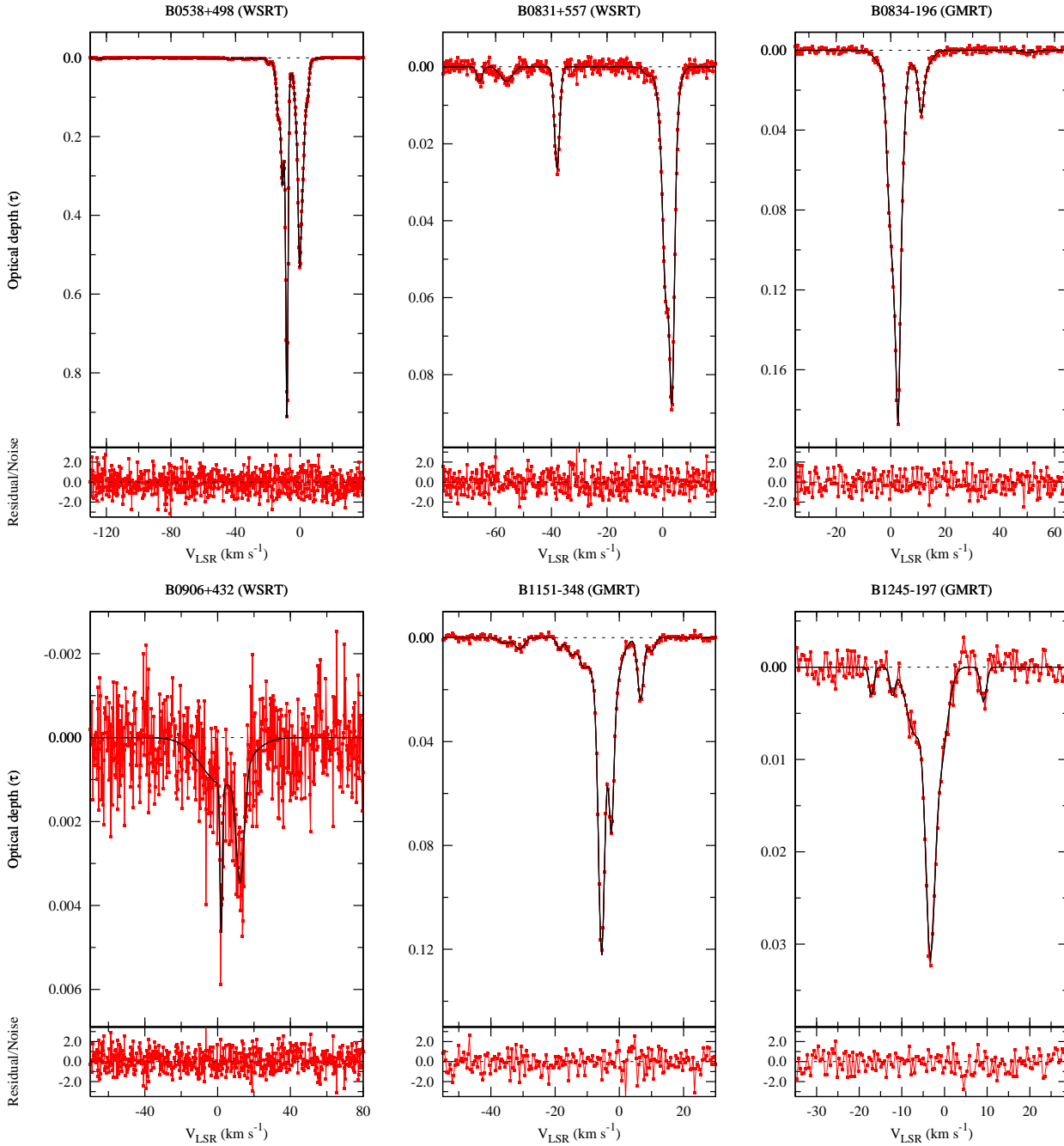


**Figure 3.** (contd.) H I 21 cm absorption spectra and multi-Gaussian fits for the 30 sources of the sample.

functional form. It is probably fair to say that, at present, these approaches are less physically motivated than a Gaussian decomposition. Finally, while much progress has been made in hydrodynamic simulations of the ISM (e.g. Gazol et al. 2001; Audit & Hennebelle 2005; Vázquez-Semadeni et al. 2006; Hennebelle & Audit 2007; Audit & Hennebelle 2010; Saury et al. 2013), the complexity of the problem has meant that such studies have unfortunately not yielded much information on realistic models of interstellar gas clouds.

In summary, while there are certainly possible drawbacks to using Gaussian components to model H I 21 cm spectra, there is no obvious alternative route to determining physical conditions in the ISM. Further, given the problems associated with single-dish

H I 21 cm emission spectra (e.g. Kanekar et al. 2003), it is important to apply a multi-Gaussian component model to the “cleaner” H I 21 cm absorption profiles to test whether these too yield a large fraction of unstable atomic gas in the ISM. This is the broad approach we follow in this paper, using a Gaussian decomposition to determine the distribution of H I kinetic temperatures, and to test whether a significant fraction of the neutral ISM is in the unstable phase.

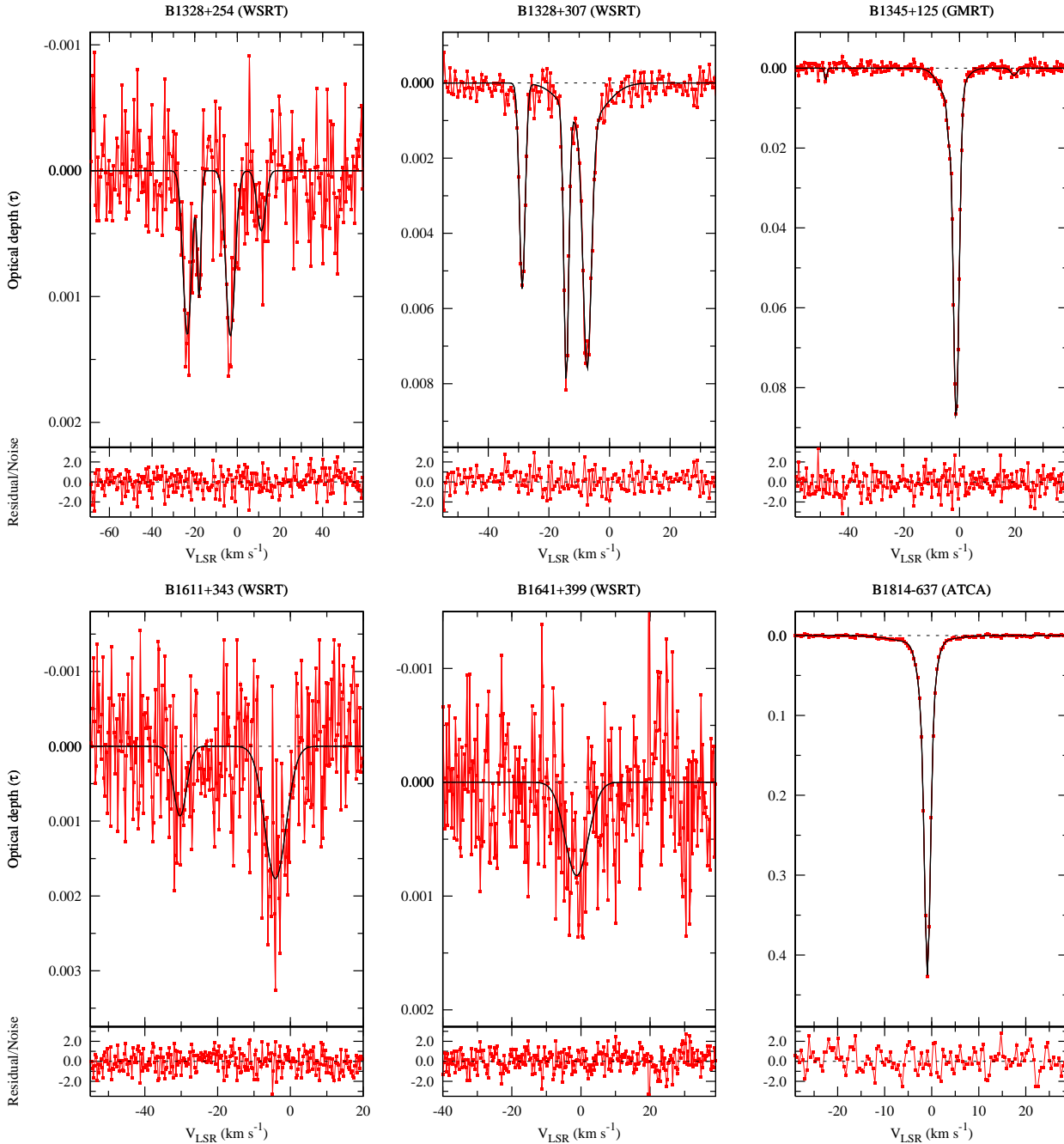


**Figure 3.** (contd.) HI-21 cm absorption spectra and multi-Gaussian fits for the 30 sources of the sample.

### 5.1 The multi-Gaussian fits

As discussed in Paper I (see Section 2.3), the noise is not uniform across each absorption spectrum, but is higher at velocity ranges containing Galactic HI-21 cm emission, which contributes to the system temperature in these velocity channels. This was taken into account to derive optical depth noise spectra for each target source. We then carried out an iterative multi-Gaussian fit to each of the 33 optical depth spectra with detected HI-21 cm absorption (i.e. excluding the sightline towards B0438–436) using the noise spectrum for the sightline, and the standard technique of  $\chi^2$ -minimization, using the Levenberg-Marquardt algorithm. For each spectrum, the number of Gaussian components was increased (beginning with a

single component) until the reduced chi-square ( $\chi_r^2$ ) was as close to unity as possible, with noise-like residuals. For three sources (B0355+508, B0429+415 and B2348+643), the absorption profiles are extremely complex and impossible to fit with a reasonable number ( $\lesssim 20$ ) of spectral components. We have hence dropped these three spectra from the multi-component analysis, thus retaining 30 sources in the final sample of sources for which the multi-Gaussian fits were found to be successful.

For each sightline, we verified through a Kolmogorov-Smirnov rank-1 test and an Anderson-Darling test that the residual spectrum after subtracting out the fitted model was consistent with a normal distribution (within  $3\sigma$  significance in each test). Since



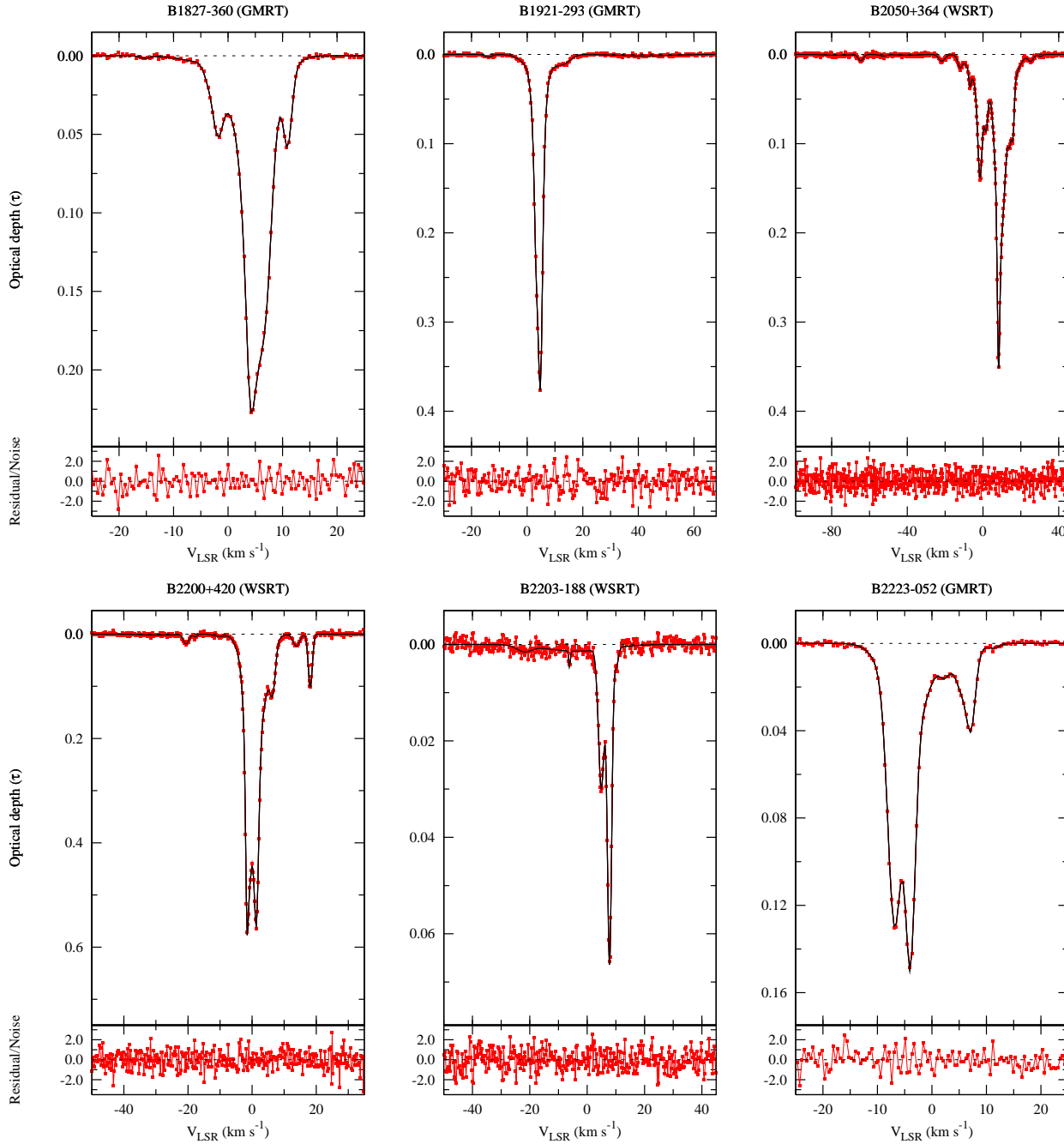


**Figure 3.** (contd.) H I-21 cm absorption spectra and multi-Gaussian fits for the 30 sources of the sample.

the noise is channel-dependent, these tests were carried out after scaling the residual spectrum by the noise spectrum (i.e. on the residual spectrum in S/N units). For all fits, we obtained  $\chi_r^2 \approx 1$  (with  $0.76 < \chi_r^2 < 1.29$  in all cases), indicating that the fitted model is a good representation of the observed H I-21 cm optical depth spectrum. Following standard procedures to obtain error estimates, the uncertainties of the fit parameters were derived after scaling the errors so as to obtain  $\chi_r^2 = 1$ . The number of fitted components in each spectrum ranges from 1 (for B0023–263, B0117–155 and B1641+399) to 20 (for B0538+498), with a median number of 7.

The above fitting procedure yielded estimates for the peak optical depths, central velocities and line FWHMs ( $\Delta V$ ) for the dif-

ferent Gaussian components. The doppler temperature  $T_D$  of each component was then obtained from the expression

$$T_D = 21.855 \times \Delta V^2 . \quad (3)$$

We emphasize that this is an *upper limit* to the kinetic temperature of each component.

For each of the 30 sightlines, the fitted multi-Gaussian model is overlaid on the optical depth spectrum in the upper panel of each plot in Fig. 3, while the lower panel of each plot shows the residual (S/N) spectrum (after dividing the residuals by the RMS optical depth noise). Fig. 4 shows the H I-21 cm absorption profiles of the three sources (B0355+508, B0429+415 and B2348+643) whose

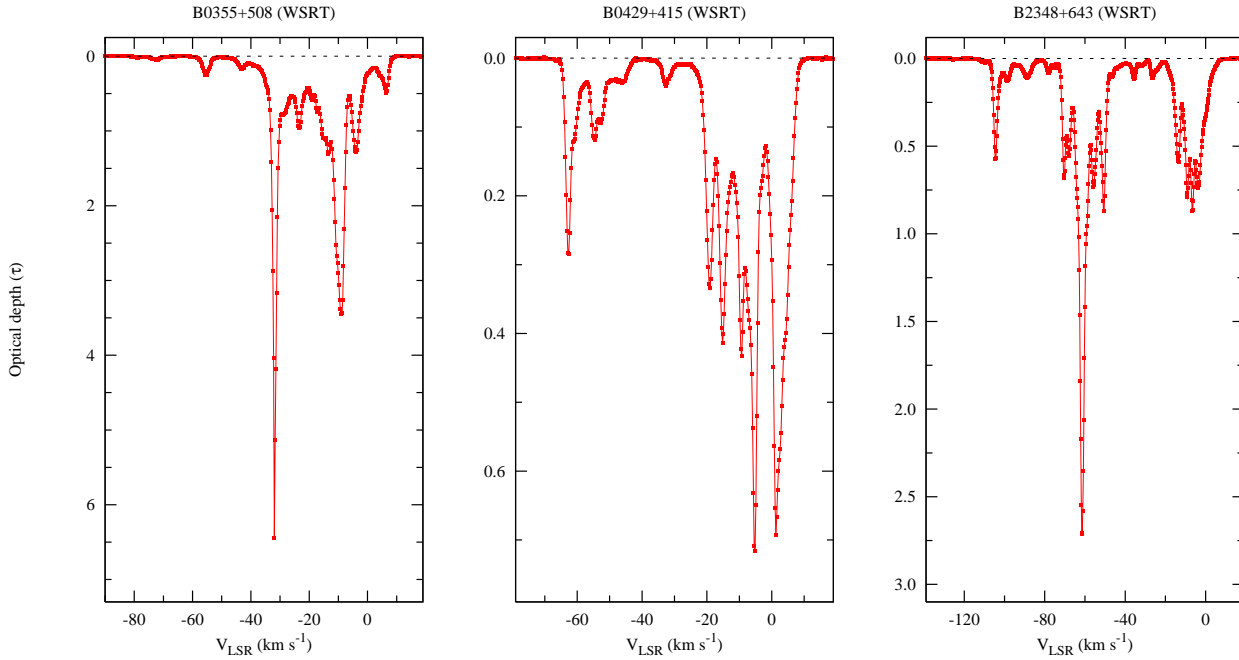


**Figure 4.** H I-21 cm absorption spectra for the three sources (B0355+508, B0429+415 and B2348+643), whose H I-21 cm profiles were found to be too complex to obtain a reliable fit.

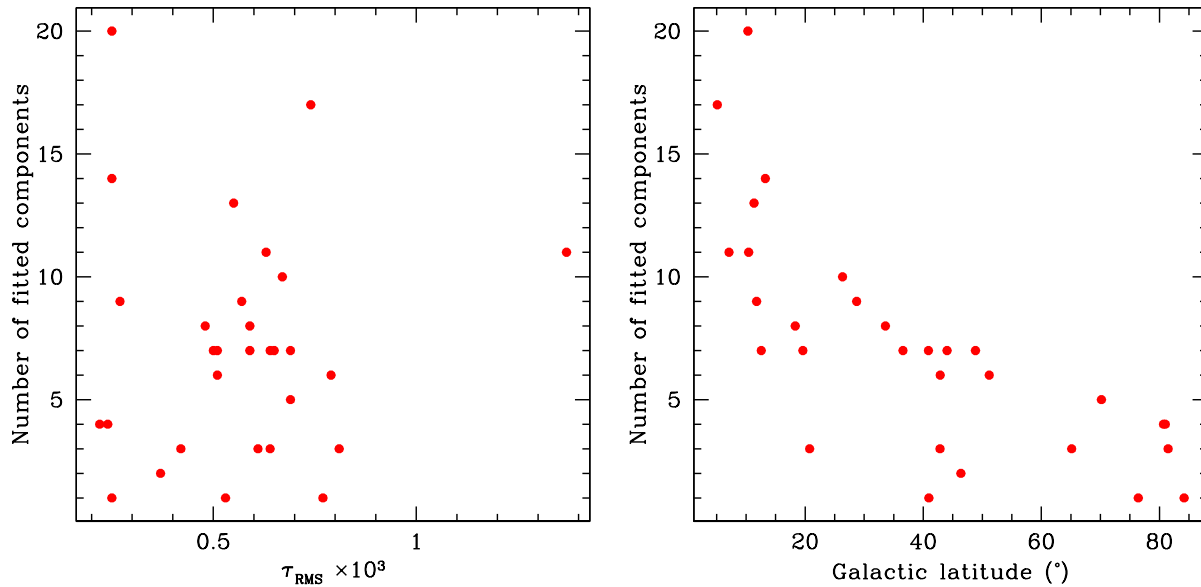


**Figure 5.** The number of fitted Gaussian components plotted versus [A] (left panel) the off-line RMS optical depth noise of each spectrum and [B] (right panel) the absolute Galactic latitude. See text for discussion.

spectra were found to be too complex to obtain a reliable fit. Finally, Table A1 in the Appendix contains the fit parameters and errors, the  $\chi_r^2$  values and the derived doppler temperatures and errors. Note that the errors on the doppler temperatures have been corrected for the minor deviations from  $\chi_r^2$  from unity.

It is interesting to ask whether the fitted multi-Gaussian profiles provide a realistic model of conditions in the ISM (e.g. whether each Gaussian component represents an H I “cloud”) or whether they merely provide a tool by which to fit a complicated

profile. In the latter situation, one would expect that the number of Gaussians needed to fit a profile would increase with decreasing RMS optical depth noise, as more and more complex structure would become apparent with improved sensitivity. One would then expect an anti-correlation between the number of fitted components and the off-line RMS optical depth noise. Fig. 5[A] plots the number of fitted components against the off-line RMS optical depth noise (at a uniform velocity resolution of  $1 \text{ km s}^{-1}$ ) for the 30 sightlines of the sample. It is clear from the figure that the number

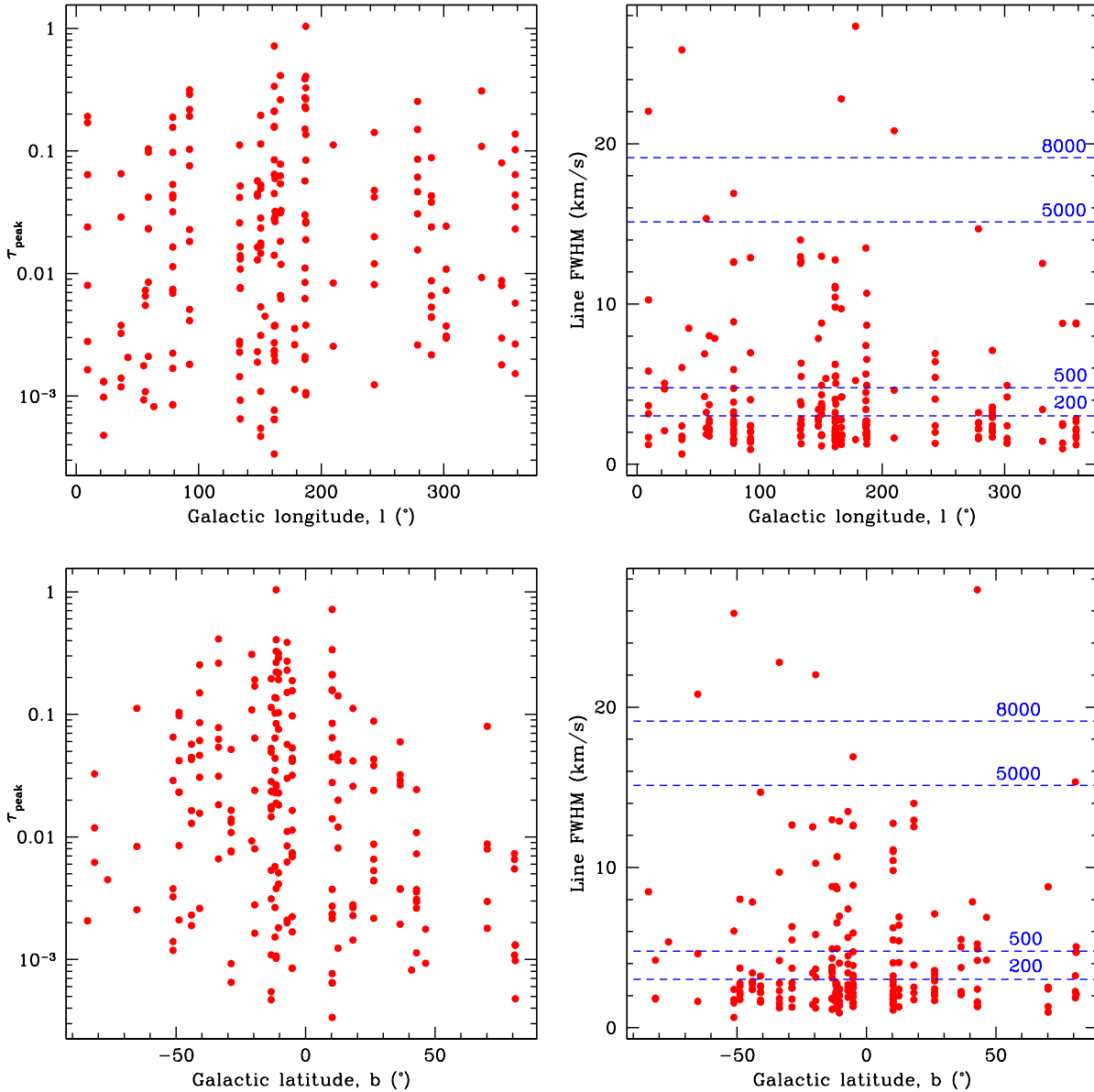


**Figure 6.** Distribution of component parameters (peak optical depth and velocity FWHM) with Galactic longitude and latitude. The horizontal dashed lines on the left panels indicate the velocity FWHMs corresponding to kinetic temperatures  $T_K = 200, 500, 5000$  and  $8000$  K. See text for discussion.

of components is not related to the RMS optical depth noise: for example, the two most sensitive spectra, towards B1328+254 and B1328+307 (with  $\tau_{\text{RMS}} \approx 0.00022\text{--}0.00024$  per  $1 \text{ km s}^{-1}$  channel), require only 4 Gaussian components, while the spectrum towards B1641+399 (with  $\tau_{\text{RMS}} \approx 0.00025$  per  $1 \text{ km s}^{-1}$  channel) requires a single Gaussian component for a good fit.

It also appears plausible that low-latitude sightlines would traverse more H I clouds, while high-latitude sightlines would only intersect a few clouds. One would then expect more components along low-latitude sightlines and fewer components along high latitude ones, independent of the sensitivity of the spectra. Fig. 5[B] plots the number of components versus the absolute Galactic latitude; it is clear from the figure that far more components are required to obtain a good fit for low latitudes,  $b \lesssim 15^\circ$ , than at high latitudes. Specifically, all sightlines with  $b \geq 15^\circ$  are well fitted

with  $\leq 10$  components, while all sightlines with  $b \geq 40^\circ$  are well fitted with  $\leq 7$  components. Conversely, all sightlines with  $b \lesssim 10^\circ$  require  $> 10$  components to obtain a good fit. We note, in passing, that the three sightlines which were excluded from the sample due to profile complexity were all at low latitudes,  $b < 10^\circ$ .

Both the above results suggest that the fitted multi-Gaussian profiles may provide a realistic model for the sightlines in our sample. We note, however, that this may break down for the most complicated profiles, with  $\geq 10$  components.

## 6 DISCUSSION

### 6.1 Component statistics

A total of 214 Gaussian components were detected in the 30 H I-21 cm absorption spectra, with the typical model consisting of several narrow components (which could be interpreted as arising in the CNM) and a few wide components (suggestive of absorption in warm gas). Note that, as argued in section 4, the spectra must contain absorption from gas with spin temperatures significantly higher than those typical of the CNM. Following Heiles & Troland (2003a), we will in this section refer to components with  $T_k \leq 500$  K as arising in the CNM, to include possible effects of non-thermal broadening. Components with  $500 \text{ K} \leq T_k \leq 5000$  K will be assumed to arise in the “unstable” phase, and components with  $T_k > 5000$  K in the WNM.

We then find that  $\sim 72\%$  of the Gaussian components arise in the CNM,  $\sim 25\%$  in the “unstable” phase and  $\sim 3\%$  in the WNM. We emphasize that we are merely counting components here, and not H I column densities; this does *not* imply that 72% of the H I along our sightlines is in the CNM! If the analysis is restricted to sightlines with “simple” absorption profiles (defined here as having 7 or fewer Gaussian components, i.e. equal to or lower than the median number for the sample), there are a total of 93 components, of which  $\sim 69\%$ ,  $\sim 26\%$  and  $\sim 5\%$  are in the cold, unstable, and warm phases, respectively. Given that our spectra are sufficiently sensitive to detect gas in the classical WNM, it is somewhat surprising that we find so few components that are unambiguously in the warm phase. Interestingly, we also find that 14 (i.e.  $\sim 7\%$ ) of the 214 components have kinetic temperatures  $T_k < 40$  K, i.e. below of the nominal temperature range of the the CNM phase. Such components have been detected in earlier studies (e.g. Heiles & Troland 2003a; Dickey et al. 2003). A simple explanation of their existence, in the context of two-phase models, is that photo-electric heating by the ejection of electrons from dust grains and polycyclic aromatic hydrocarbons is not important in these clouds, perhaps due to a lack of such large molecules (Wolfire et al. 1995; Heiles & Troland 2003b).

### 6.2 Trends with Galactic latitude and longitude

The absorption spectra of our sample cover a wide range of Galactic ( $l, b$ ) values. The derived results from the sample are an average over all these sightlines, and are thus likely to sample a range of local conditions (e.g. density, pressure, background radiation field, etc). While the sample is as yet too small to test for variations of the derived parameters (e.g. the CNM fraction) with direction, we examine here whether the distribution of these parameters shows any striking trend with Galactic co-ordinates.

The distribution of peak optical depth,  $\tau_{\text{peak}}$ , and velocity FWHM for the 214 absorption components is plotted versus Galactic latitude and longitude in the four panels of Fig. 6. Larger peak optical depths are obtained at low Galactic latitudes (as expected), and also for sightlines near the Galactic anti-centre. The latter is interesting because the cold gas content is expected to decrease in the outskirts of the Galaxy, yielding lower peak optical depths. Of course, this is partly compensated for by the clustering in velocity space towards the anti-centre. Similarly, the typical number of components required to fit the profile increase as one approaches the Galactic plane. However, there is no significant correlation of the component widths with  $l$  or  $b$ . This indicates that the widths of the individual absorption components do not have a significant contribution from Galactic rotation.

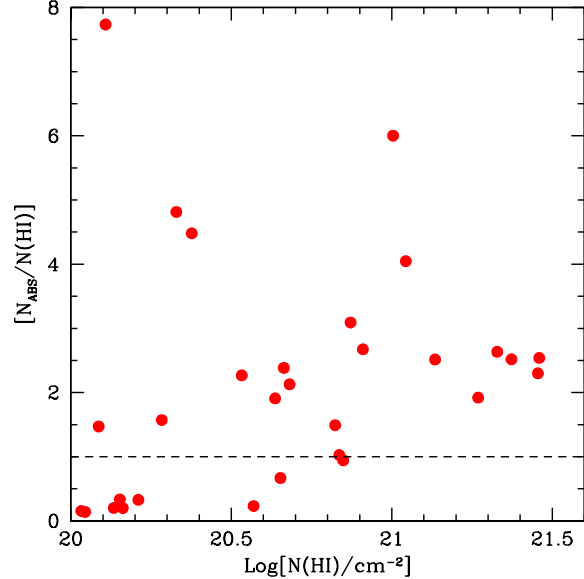


**Figure 7.** The figure shows the ratio  $N_{\text{ABS}}/N(\text{HI})$  plotted against  $\text{Log}[N(\text{HI})]$  for each of the 30 sightlines, where  $N_{\text{ABS}}$  is the H I column density derived from the fits to the absorption profile and  $N(\text{HI})$  is the H I column density derived from the LAB emission profile, in the optically-thin limit. The ratio is typically  $\approx 2$ , except for a few low- $N(\text{HI})$  sightlines. See discussion in Section 6.3.

### 6.3 Non-thermal broadening

A test of the presence of non-thermal broadening within the Gaussian parametrisation can be carried out by comparing, for each sightline, the total H I column density derived from the fit to the absorption spectrum  $N_{\text{ABS}}$  with the H I column density  $N(\text{HI})$  measured from the LAB emission spectrum. The total H I column density along a sightline from the Gaussian fit is given by the expression

$$N_{\text{ABS}} = \sum_i 1.823 \times T_{s,i} \times 1.06 \times \tau_{\text{peak},i} \times \Delta V_i, \quad (4)$$

where  $\Delta V_i$  and  $\tau_{\text{peak},i}$  are the FWHM and the peak optical depth of the  $i$ 'th component, respectively. Note that the Gaussian fit only yields the *doppler* temperature  $T_D$ , and not the *spin* temperature  $T_s$ . Assuming  $T_s = T_D$  for each component yields an upper limit to its H I column density, as  $T_D \geq T_k$  and  $T_k \geq T_s$ . Adding the contributions of all components along a sightline in equation (4) then gives an upper limit to the total H I column density detected in absorption,  $N_{\text{ABS}}$ , for the sightline.

The ratio  $N_{\text{ABS}}/N(\text{HI})$  is then an upper limit to the ratio of the H I column density detected in H I-21 cm absorption to the total H I column density. Of course, if only a small fraction of the total gas along a given sightline is detected in H I-21 cm absorption,  $N_{\text{ABS}}$  could be *lower* than  $N(\text{HI})$ . Conversely, if non-thermal motions contribute to the component FWHMs, then the inferred doppler temperatures would be larger than the kinetic temperatures, which are, in turn, larger than or equal to the spin temperatures. This would imply that  $N_{\text{ABS}}$  would be *larger* than  $N(\text{HI})$ . In other words, a scenario wherein the H I column density derived from the absorption fits is systematically larger than the H I column measured from the emission profile is indicative of non-thermal broadening (and/or that the spin temperature is lower than the kinetic temperature).

Fig. 7 plots the ratio  $R \equiv N_{\text{ABS}}/N(\text{H I})$  against  $N(\text{H I})$ . Ten sightlines out of thirty have  $R \leq 1$ , as would be expected if non-thermal motions do not contribute appreciably to the component widths. However, fifteen sightlines have  $R \approx 1.5 - 3$ , while five sightlines have  $R \approx 4 - 7.7$ . We conclude that non-thermal broadening is likely to be present for twenty of the thirty sightlines. The median value of the ratio  $N_{\text{ABS}}/N(\text{H I})$  is  $\approx 2.0$ . Note that this deviation from unity includes contributions both from non-thermal broadening and from the possibility that  $T_s < T_k$ . Thus, it appears that the contribution to the component widths from non-thermal broadening is larger than the thermal width by a factor  $\lesssim \sqrt{3}$ , and does not dominate the line widths.

Finally, one might infer the fraction of H I in different phases of the ISM from the H I column densities derived from the multi-Gaussian fits to the absorption profiles, as done by Kanekar et al. (2003). However, this requires one to use the doppler temperatures to differentiate between the CNM, WNM and thermally unstable neutral medium. Of course, the critical missing ingredient is the extent of non-thermal broadening of individual line components. For example, a significant fraction of absorption with doppler temperatures in the unstable range might arise from non-thermally broadened CNM absorption. We note that this is the approach followed by Heiles & Troland (2003b), based on their multi-Gaussian decomposition of the H I-21 cm absorption and emission profiles, to infer that around one-third of all H I is in the thermally unstable phase. While Heiles & Troland (2003b) identified all components that were not detected in absorption with the WNM, non-thermal broadening would reduce the strength of any absorption, possibly causing it to not be detected. It is hence difficult to disentangle the results of Heiles & Troland (2003b) and Kanekar et al. (2003) from the effects of non-thermal broadening. In the next section, we will attempt to more rigorously examine the presence or absence of unstable gas in the ISM.

#### 6.4 The two-phase model of the neutral ISM

In Section 4 we showed that the detected H I-21 cm absorption cannot arise solely in gas with spin temperatures in the CNM range, but must include absorption from warmer gas. In other words, it is reasonable to associate wide components that are found in the Gaussian decomposition of our spectra with warm gas, as opposed to non-thermally broadened CNM. In the classic two-phase models, this additional absorption can only arise in stable WNM. However, only  $\approx 5\%$  of the Gaussian components have kinetic temperatures consistent with values expected in the WNM. Fig. 8 compares the maximum kinetic temperature obtained along each sightline ( $T_{k,\text{Max}}$ ) to the stable WNM temperature range. It is clear that only five sightlines have maximum inferred kinetic temperatures consistent with absorption by stable WNM ( $5000 \leq T_k \leq 8000$  K), within  $1\sigma$  significance. An additional nine sightlines have maximum inferred kinetic temperatures consistent with the above temperature range within  $3\sigma$  significance. Even if we include all of these as possible WNM components, there are sixteen sightlines where the highest doppler temperature is significantly lower than the stable range of WNM temperatures.

For the sixteen sightlines with no detected absorption component with  $T_D$  in the stable WNM range, it is possible that all the observed H I-21 cm absorption arises in non-thermally broadened CNM. Assuming that such non-thermally broadened CNM has a spin temperature of 200 K yields an upper limit to the CNM column density along each sightline. If the H I indeed exists in two stable phases, the CNM and the WNM, with no gas in the ther-

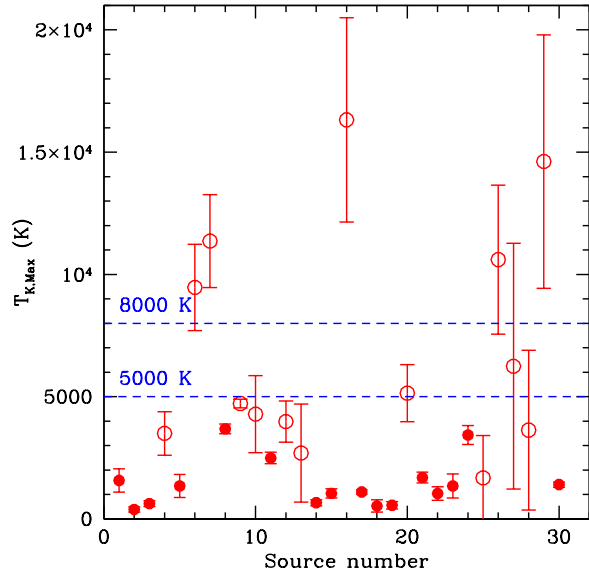


**Figure 8.** The maximum kinetic temperature of the different components on each of the 30 sightlines, from the multi-Gaussian fits; the stable WNM temperature range (5000 – 8000 K) is indicated by the horizontal dashed lines. Components with temperatures consistent with stable WNM are indicated by open circles, while those definitely outside the above range (at  $\geq 3\sigma$  significance) are shown as filled circles. See Section 6.4 for discussion.

mally unstable phase, then the rest of the H I detected in the H I emission spectrum on each sightline must be stable WNM. Following the arguments in Section 4, one can immediately test whether this residual H I would have been detected in the H I-21 cm absorption spectrum. For this purpose, we again assume, conservatively, that the WNM has  $T_s = 5000$  K and a line FWHM =  $\Delta V_{90}$ .

These results are summarized in Table 2 whose columns are (1) the source name, (2) the total H I column density, from the isothermal estimate  $N(\text{H I})$ , (3) the upper limit to the CNM column density,  $N_{\text{CNM}}$ , for  $T_s = 200$  K, (4) the upper limit to the CNM fraction along the sightline, using the ratio  $N_{\text{CNM}}/N(\text{H I})$ , (5) the maximum kinetic temperature measured along the sightline, (6) for the sixteen systems with no absorption components corresponding to stable WNM, the S/N at which the residual H I would have been detected, for line FWHM =  $\Delta V_{90}$  and  $T_s = 5000$  K, (7) for these sightlines, the upper limit to the fraction of H I in the stable WNM (assuming a  $3\sigma$  detection significance), and (8) for these sightlines, the lower limit to the fraction of H I in the unstable phase, assuming that all the H I-21 cm absorption arises in the CNM and that the WNM column is just below the  $3\sigma$  detection threshold for H I-21 cm absorption. Sources with detected WNM components are listed as “WNM” in the sixth column and “-” in the last column of the table.

We emphasize that the assumptions are extremely conservative, using (1) the highest spin temperature in the CNM range, (2) the highest spin temperature expected in the WNM temperature range (Liszt 2001), and (3) assuming extreme non-thermal broadening of the putative WNM components. All of these would reduce the strength (and hence the detection S/N) of the expected WNM absorption. Even with these assumptions, we find that H I-21 cm absorption would have been detected at  $\geq 3\sigma$  significance on thirteen of the sixteen sightlines if the residual gas along the sightline

**Table 2.** Evidence for gas in the unstable temperature range. See text for discussion.

Source	N(H I) $\times 10^{20} \text{ cm}^{-2}$	N <sub>CNM</sub> $\times 10^{20} \text{ cm}^{-2}$ T <sub>s</sub> = 200 K	f <sub>CNM</sub> *	T <sub>K,Max</sub> <sup>†</sup> K	S/N <sup>‡</sup>	f <sub>WNM</sub> **	f <sub>UNM</sub> ***
B0023-263	1.62	0.093	0.06	1574 ± 473	3.0	0.95	0.00
B0114-211	1.42	0.494	0.35	388 ± 106	1.5	1.00	0.00
B0117-155	1.45	0.112	0.08	627 ± 114	3.0	0.92	0.00
B0134+329	4.33	1.615	0.37	3497 ± 890	WNM	0.12	-
B0202+149	4.80	2.724	0.57	1347 ± 475	8.8	0.15	0.29
B0237-233	2.13	1.071	0.50	9468 ± 1767	WNM	0.47	-
B0316+162	10.09	10.810	1.00	11364 ± 1898	WNM	0.07	-
B0316+413	13.64	7.077	0.52	3683 ± 196	38.8	0.04	0.44
B0404+768	11.06	7.091	0.64	4718 ± 182	WNM	0.17	-
B0407-658	3.41	1.998	0.59	4285 ± 1576	WNM	0.43	-
B0518+165	23.60	22.750	0.96	2491 ± 235	2.4	0.04	0.00
B0531+194	28.80	14.810	0.51	3980 ± 841	WNM	0.04	-
B0538+498	21.31	20.480	0.96	2693 ± 2004	WNM	0.03	-
B0831+557	4.50	1.761	0.39	664 ± 124	5.6	0.33	0.28
B0834-196	6.86	3.548	0.52	1045 ± 186	6.0	0.24	0.24
B0906+430	1.28	0.187	0.15	16320 ± 4179	WNM	0.94	-
B1151-348	7.06	2.603	0.37	1104 ± 91	6.1	0.31	0.32
B1245-197	3.71	0.576	0.16	529 ± 249	5.6	0.46	0.38
B1328+254	1.11	0.078	0.07	559 ± 149	5.5	0.51	0.42
B1328+307	1.22	0.261	0.21	5143 ± 1168	WNM	0.38	-
B1345+125	1.92	1.112	0.58	1691 ± 220	2.1	0.60	0.00
B1611+343	1.36	0.068	0.05	1037 ± 278	4.5	0.64	0.31
B1641+399	1.08	0.032	0.03	1350 ± 492	5.0	0.58	0.39
B1814-637	6.66	3.637	0.55	3433 ± 388	7.8	0.17	0.28
B1827-360	8.13	5.622	0.69	1678 ± 1731	WNM	0.15	-
B1921-293	7.44	5.272	0.71	10605 ± 3046	WNM	0.19	-
B2050+364	28.53	11.030	0.39	6246 ± 5027	WNM	0.07	-
B2200+420	18.59	13.010	0.70	3632 ± 3267	WNM	0.20	-
B2203-188	2.38	0.905	0.38	14617 ± 5183	WNM	0.43	-
B2223-052	4.61	3.770	0.82	1405 ± 105	3.6	0.15	0.03

† The kinetic temperature of the widest fitted component along each sightline. In the case of B0538+498 and B1827-360, the listed component has a lower doppler temperature than that of another component along the sightline (which have T<sub>k</sub> = 3552 ± 342 K and T<sub>k</sub> = 1699 ± 165 K, respectively). However, the 1σ error is larger for the listed components, due to which their kinetic temperatures are formally consistent with the WNM range. We have hence chosen to list these components in the table.

‡ The signal-to-noise ratio at which residual H I (i.e. after subtracting out N<sub>CNM</sub>) would have been detected in our H I-21 cm absorption spectra, for an assumed T<sub>s</sub> = 5000 K and line FWHM = ΔV<sub>90</sub>. Systems with detected WNM components are listed as “WNM” in this column.

\* The upper limit to the fraction of gas in the CNM phase along the sightline, assuming that all the absorption arises in CNM with a spin temperature of 200 K.

\*\* The upper limit to the fraction of gas in the stable WNM phase along the sightline, for a 3σ detection significance, assuming T<sub>s</sub> = 5000 K and line FWHM = ΔV<sub>90</sub>.

\*\*\* The lower limit to the fraction of gas in the unstable phase (200 < T<sub>k</sub> < 5000 K), assuming that all detected H I-21 cm absorption arises in the CNM and that there is stable WNM along the sightline just below the 3σ detection threshold for absorption. This is essentially 1 - (f<sub>CNM</sub> + f<sub>WNM</sub>). For sources with detected WNM components, this column contains a “-”.

was in the stable WNM phase (and at ≥ 4.5σ significance on ten of the sightlines). In other words, for these thirteen sightlines, if all the residual gas is WNM, the multi-Gaussian fit would have included at least one component with doppler temperature at or above the stable WNM range. Thus, the spectra of thirteen (i.e. ~ 43%) out of the thirty sightlines are inconsistent with a model in which neutral gas exists in only the stable temperature ranges of the two-phase models. We conclude that, along these thirteen sightlines, much of the difference between the total H I column density and the upper limit to the CNM column density must arise in gas in the thermally unstable phase.

The non-detection of WNM components along the above thirteen sightlines can be used to place an upper limit on the WNM column density along these sightlines, and hence, to obtain a 3σ upper limit on the WNM fraction f<sub>WNM</sub>. We also already have an

upper limit to the CNM column density and the CNM fraction along these sightlines by assuming that all the detected H I-21 cm absorption arises in cold gas with T<sub>s</sub> = 200 K. The difference between the total H I column density and the sum of these *upper limits* on the WNM and CNM column densities then yields a *lower limit* to the column density of gas in the unstable neutral medium, and thus, a lower limit to the fraction f<sub>UNM</sub> of the gas in the unstable phase (at 200 K < T<sub>k</sub> < 5000 K). The latter lower limits are listed in the last column of Table 2. For the above thirteen sightlines where stable WNM would, if present, have been detected at ≥ 3σ significance, the lower limits to the fraction of unstable gas lie in the range 0.00 < f<sub>UNM</sub> < 0.44, with a median value of ≈ 0.28. We emphasize that these are *lower limits* to f<sub>UNM</sub>. The assumption that all the observed H I-21 cm absorption arises in the CNM is obviously incorrect, since H I-21 cm absorption from gas in the

unstable phase would have lower spin temperatures and velocity widths than absorption by stable WNM, and would hence have been detected at higher significance. Indeed, each of the thirteen sightlines contains at least one component with doppler temperature in the range  $200 \text{ K} < T_D < 5000 \text{ K}$ . Thus, some of the observed H I-21 cm absorption must arise in gas in the unstable temperature range. In addition, the high assumed CNM spin temperature implies that the listed CNM fractions are all stringent upper limits. Finally, the WNM fractions are also stringent upper limits because we have assumed that the WNM column density is just below our  $3\sigma$  detection threshold, for  $T_s = 5000 \text{ K}$  and line FWHM  $= \Delta V_{90}$ . *We hence conclude that a significant fraction of the gas, typically  $\geq 28\%$ , must be present in the unstable phase along thirteen of our sightlines, and that the “classic” two-phase model is not viable for at least these sightlines.* We also note, in passing, that it is likely that many of the remaining seventeen sightlines also contain thermally unstable gas, given that almost all of them contain absorption with  $T_D$  in the range  $500 < T_D < 5000 \text{ K}$ .

For comparison, Heiles & Troland (2003b) found  $> 30\%$  of the H I along their sightlines to have temperatures in the unstable range (which they defined as  $500 \text{ K} < T_D < 5000 \text{ K}$ ), in reasonable agreement with our results. This is curious, given the fact that their derived fractions in different phases would be seriously affected by non-thermal broadening, which was not accounted for in their analysis. Note that our analysis explicitly takes into account the possibility of contributions from non-thermal broadening to the line widths, via the conservative assumption that the WNM line widths are equal to  $\Delta V_{90}$ , the width of the H I-21 cm emission profile that contributes 90% of the H I-21 cm emission.

## 7 CONCLUSIONS

We have studied the temperature distribution of the neutral interstellar medium along 33 Galactic sightlines, using deep, high velocity resolution ( $\approx 0.26 - 0.52 \text{ km s}^{-1}$ ) H I-21 cm absorption spectra obtained with the WSRT, the GMRT and the ATCA. The typical RMS optical depth noise of the spectra is  $\lesssim 10^{-3}$  per  $1 \text{ km s}^{-1}$  velocity channel, making the spectra sufficiently sensitive to detect H I-21 cm absorption from gas in the warm neutral medium, with H I column densities  $\geq 10^{20} \text{ cm}^{-2}$  and velocity widths comparable to the thermal width.

We used conservative assumptions regarding the CNM spin temperature ( $T_s = 200 \text{ K}$ ), the WNM spin temperature ( $T_s = 5000 \text{ K}$ ) and non-thermal broadening of the WNM (line FWHM  $= \Delta V_{90}$ ) to consider the canonical two-phase model of the ISM wherein the H I-21 cm absorption features arise in the CNM, while the emission profiles contain contributions from both stable CNM and WNM. We find that such a model can be ruled out for more than half our sightlines. Some of the H I-21 cm absorption that we detect *must* arise from gas with spin temperatures larger than that of the CNM (i.e. must arise in the WNM or with gas with temperatures in the thermally unstable range).

We then used a multi-Gaussian decomposition of 30 of the H I-21 cm absorption spectra to examine the possibility that some Galactic H I might be in the unstable temperature range,  $200 < T_k < 5000 \text{ K}$ . We found very few components with doppler line widths consistent with values expected from stable or non-thermally broadened WNM. For sixteen sightlines, we found no H I-21 cm absorption components with line widths consistent with an origin in the WNM. Thirteen of the sixteen spectra are sufficiently sensitive to detect any WNM along the sightline even if ex-

treme non-thermal broadening results in line FWHMs comparable to the  $\Delta V_{90}$  of the H I-21 cm emission profile. We can thus rule out the possibility that the neutral hydrogen along these sixteen sightlines is in two phases, with temperatures in the stable CNM and WNM ranges. Some fraction of the H I-21 cm absorption that we detect on these sightlines must arise from gas with temperatures in the intermediate, thermally unstable range (at  $200 \text{ K} < T_k < 5000 \text{ K}$ ) of the two-phase model. For the above thirteen sightlines, we obtain a median lower limit of 28% to the gas fraction in this unstable phase. Our observations hence robustly indicate that a significant fraction of the gas in the Galactic ISM has a temperature outside the thermally stable ranges in two-phase models.

## ACKNOWLEDGEMENTS

This research has made use of the NASA’s Astrophysics Data System. We thank Robert Braun for useful discussions and his comments on an earlier version of the paper. We are very grateful to Harvey Liszt for providing us his simulation results, and to Ranjeev Misra, Rajaram Nityananda, Sanjay Bhatnagar and A. Pramesh Rao for many helpful comments. We thank the staff of the GMRT and the WSRT who have made these observations possible. The GMRT is run by the National Centre for Radio Astrophysics of the Tata Institute of Fundamental Research. The WSRT is operated by ASTRON (the Netherlands Institute for Radio Astronomy), with support from the Netherlands Foundation for Scientific Research (NWO). Some of the data used in this paper were obtained from the Leiden/Argentine/Bonn Galactic H I Survey. NR acknowledges the Jansky Fellowship Program of NRAO/NSF/AUI and support from the Alexander von Humboldt Foundation. NR also acknowledges support from NCRA during his Ph.D., when a significant fraction of this work was done. NK acknowledges support from the Department of Science and Technology through a Ramanujan Fellowship.

## REFERENCES

- Audit E., Hennebelle P., 2005, A&A, 433, 1
- Audit E., Hennebelle P., 2010, A&A, 511, 76
- Bajaja E., Arnal E. M., Larrarte J. J., Morras R., Pöppel W. G. L., Kalberla P. M. W., 2005, A&A, 440, 767
- Braun R., Kanekar N., 2005, A&A, 436, L53
- Chengalur J. N., Kanekar N., Roy N., 2013, MNRAS, 432, 3074
- Clark B. G., Radhakrishnan V., Wilson R. W., 1962, ApJ, 135, 151
- Dickey J. M., McClure-Griffiths N. M., Gaensler B. M., Green A. J., 2003, ApJ, 585, 801
- Dickey J. M., Terzian Y., Salpeter E. E., 1978, ApJS, 36, 77
- Field G. B., 1965, ApJ, 142, 531
- Field G. B., Goldsmith D. W., Habing H. J., 1969, ApJ, 155, L149
- Gazol A., Vázquez-Semadeni E., Sánchez-Salcedo F. J., Scalo J., 2001, ApJ, 557, L121
- Heiles C., Troland T. H., 2003a, ApJS, 145, 329
- Heiles C., Troland T. H., 2003b, ApJ, 586, 1067
- Hennebelle P., Audit E., 2007, A&A, 465, 431
- Kalberla P. M. W., Burton W. B., Hartmann D., Arnal E. M., Bajaja E., Morras R., Pöppel W. G. L., 2005, A&A, 440, 775
- Kanekar N., Braun R., Roy N. 2011, ApJ, 737, L33
- Kanekar N., Ghosh T., Chengalur J. N., 2001, A&A, 373, 394
- Kanekar N., Subrahmanyan R., Chengalur J. N., Safouris V., 2003, MNRAS, 346, L57

Kulkarni S. R., Heiles C., 1988, in Verschuur G. L., Keller-  
mann K. I., eds, Galactic and Extra-Galactic Radio Astronomy  
Springer-Verlag New York, p. 95  
Lane W. M., Briggs F. H., Smette A., 2000, ApJ, 532, 146  
Liszt H., 2001, A&A, 371, 698  
McKee C. F., Ostriker J. P., 1977, ApJ, 218, 148  
Mebold U., 1972, A&A, 19, 13  
Mebold U., Winnberg A., Kalberla P. M. W., Goss W. M., 1982,  
A&A, 115, 223  
Payne H. E., Terzian Y., Salpeter E. E., 1982, ApJS, 48, 199  
Radhakrishnan V., Murray J. D., Lockhart P., Whittle R. P. J.,  
1972, ApJS, 24, 15  
Roy N., Chengalur J. N., Srianand R., 2006, MNRAS, 365, L1  
Roy N., Kanekar N., Braun R., Chengalur J. N., 2013, MNRAS  
(submitted; Paper I)  
Saury E., Miville-Deschênes M.-A., Hennebelle P., Audit E.,  
Schmidt W., 2013, arXiv:1301.3446  
Vázquez-Semadeni E., Ryu D., Passot T., González R. F., Gazol  
A., 2006, ApJ, 643, 245  
Wakker B. P., Lockman F. J., Brown J. M., 2011, ApJ, 728, 159  
Wolfire M. G., Hollenbach D., McKee C. F., Tielens A. G. G. M.,  
Bakes E. L. O., 1995, ApJ, 443, 152  
Wolfire M. G., McKee C. F., Hollenbach D., Tielens A. G. G. M.,  
2003, ApJ, 587, 278

This paper has been typeset from a  $\text{\TeX}/\text{\LaTeX}$  file prepared by the  
author.

## APPENDIX A: THE RESULTS OF THE GAUSSIAN FITS

The parameters of the multi-Gaussian fits are summarised in Ta-  
ble A1. The four columns of the table list (1) the peak H<sub>1</sub>-21 cm  
optical depth  $\tau_{\text{peak}}$ , (2) the central absorption velocity  $V_c$ , in  $\text{km s}^{-1}$ ,  
(3) the  $b$ -parameter, in  $\text{km s}^{-1}$ , and (4) the doppler temperature  $T_D$ ,  
in K.

**Table A1.** The parameters of the multi-Gaussian fits.

$\tau_{\text{peak}}$	$V_c$ $\text{km s}^{-1}$	$b$ $\text{km s}^{-1}$	$T_D$ K
B0023–263 (WSRT); $N_{\text{comp}} = 1$ ; $\chi_r^2 = 0.999$ :			
$0.00207 \pm 0.00027$	$-5.09 \pm 0.54$	$5.10 \pm 0.77$	$1574 \pm 473$
B0114–211 (WSRT); $N_{\text{comp}} = 3$ ; $\chi_r^2 = 1.004$ :			
$0.0327 \pm 0.0037$	$-7.727 \pm 0.038$	$1.109 \pm 0.086$	$75 \pm 12$
$0.00620 \pm 0.00089$	$-2.07 \pm 0.14$	$1.08 \pm 0.20$	$70 \pm 26$
$0.0119 \pm 0.0038$	$-7.10 \pm 0.25$	$2.53 \pm 0.35$	$388 \pm 106$
B0117–155 (WSRT); $N_{\text{comp}} = 1$ ; $\chi_r^2 = 1.007$ :			
$0.00448 \pm 0.00035$	$-6.33 \pm 0.21$	$3.22 \pm 0.29$	$627 \pm 114$
B0134+329 (WSRT); $N_{\text{comp}} = 9$ ; $\chi_r^2 = 1.055$ :			
$0.00065 \pm 0.00024$	$19.99 \pm 0.45$	$1.49 \pm 0.64$	$135 \pm 119$
$0.0518 \pm 0.0011$	$2.258 \pm 0.013$	$1.489 \pm 0.025$	$134.4 \pm 4.7$
$0.0131 \pm 0.0014$	$-0.663 \pm 0.050$	$1.072 \pm 0.094$	$70 \pm 13$
$0.0109 \pm 0.0013$	$-2.413 \pm 0.051$	$0.774 \pm 0.083$	$36.3 \pm 8.0$
$0.0077 \pm 0.0019$	$-2.83 \pm 0.67$	$7.60 \pm 0.94$	$3497 \pm 890$
$0.0140 \pm 0.0017$	$-4.56 \pm 0.11$	$2.23 \pm 0.23$	$301 \pm 63$
$0.01651 \pm 0.00074$	$-11.104 \pm 0.038$	$1.685 \pm 0.070$	$172 \pm 15$
$0.00756 \pm 0.00040$	$-15.33 \pm 0.20$	$3.79 \pm 0.23$	$870 \pm 107$
$0.00093 \pm 0.00017$	$-29.27 \pm 0.48$	$3.29 \pm 0.68$	$656 \pm 278$
B0202+149 (WSRT); $N_{\text{comp}} = 7$ ; $\chi_r^2 = 0.923$ :			
$0.0570 \pm 0.0045$	$-10.761 \pm 0.042$	$1.434 \pm 0.052$	$124.7 \pm 8.7$
$0.0428 \pm 0.0059$	$-5.749 \pm 0.039$	$1.63 \pm 0.10$	$160 \pm 19$
$0.0164 \pm 0.0019$	$-0.120 \pm 0.071$	$1.74 \pm 0.14$	$183 \pm 28$
$0.0129 \pm 0.0060$	$-13.53 \pm 0.37$	$2.05 \pm 0.47$	$256 \pm 112$
$0.00189 \pm 0.00042$	$-52.76 \pm 0.31$	$1.72 \pm 0.44$	$180 \pm 88$
$0.0446 \pm 0.0050$	$-7.09 \pm 0.54$	$4.71 \pm 0.86$	$1347 \pm 475$
$0.00230 \pm 0.00054$	$3.79 \pm 0.32$	$1.44 \pm 0.45$	$126 \pm 76$
B0237–233 (WSRT); $N_{\text{comp}} = 3$ ; $\chi_r^2 = 0.963$ :			
$0.11190 \pm 0.00072$	$-0.0689 \pm 0.0051$	$0.9871 \pm 0.0078$	$59.07 \pm 0.91$
$0.00836 \pm 0.00051$	$-10.01 \pm 0.13$	$2.78 \pm 0.21$	$468 \pm 71$
$0.00255 \pm 0.00034$	$-4.5 \pm 1.1$	$12.5 \pm 1.2$	$9468 \pm 1767$
B0316+162 (GMRT); $N_{\text{comp}} = 8$ ; $\chi_r^2 = 1.190$ :			
$0.2614 \pm 0.0061$	$-2.666 \pm 0.050$	$1.660 \pm 0.034$	$167.0 \pm 7.6$
$0.0627 \pm 0.0028$	$6.007 \pm 0.065$	$2.518 \pm 0.085$	$384 \pm 28$
$0.0313 \pm 0.0018$	$7.025 \pm 0.023$	$0.913 \pm 0.044$	$50.5 \pm 5.4$
$0.01829 \pm 0.00056$	$-10.188 \pm 0.026$	$1.096 \pm 0.042$	$72.8 \pm 6.1$
$0.0066 \pm 0.0015$	$-1.13 \pm 0.55$	$13.7 \pm 1.0$	$11364 \pm 1898$
$0.0540 \pm 0.0028$	$0.74 \pm 0.23$	$5.83 \pm 0.25$	$2058 \pm 192$
$0.0780 \pm 0.0095$	$-1.731 \pm 0.019$	$0.747 \pm 0.043$	$33.8 \pm 4.2$
$0.4122 \pm 0.0050$	$-0.125 \pm 0.013$	$1.383 \pm 0.013$	$116.0 \pm 2.4$
B0316+413 (WSRT); $N_{\text{comp}} = 14$ ; $\chi_r^2 = 0.988$ :			
$0.00109 \pm 0.00029$	$-34.51 \pm 0.44$	$2.15 \pm 0.76$	$280 \pm 198$
$0.00047 \pm 0.00016$	$-55.78 \pm 0.72$	$2.6 \pm 1.0$	$411 \pm 318$
$0.00055 \pm 0.00019$	$-39.78 \pm 0.67$	$2.1 \pm 1.0$	$255 \pm 250$
$0.0235 \pm 0.0091$	$3.378 \pm 0.094$	$1.07 \pm 0.15$	$69 \pm 20$
$0.0492 \pm 0.0037$	$-2.155 \pm 0.065$	$1.094 \pm 0.092$	$73 \pm 12$
$0.0283 \pm 0.0032$	$0.08 \pm 0.16$	$7.79 \pm 0.21$	$3683 \pm 196$
$0.01769 \pm 0.00067$	$8.978 \pm 0.046$	$1.871 \pm 0.068$	$212 \pm 15$



**Table A1.** (continued) The parameters of the multi-Gaussian fits.

$\tau_{\text{peak}}$	$V_c$ km s <sup>-1</sup>	$b$ km s <sup>-1</sup>	$T_D$ K
B0316+413 (WSRT); $N_{\text{comp}} = 14$ ; $\chi_r^2 = 0.988$ (cont.):			
0.1952 ± 0.0068	2.20 ± 0.10	2.222 ± 0.084	299 ± 22
0.1139 ± 0.0098	-0.380 ± 0.024	1.107 ± 0.060	74.2 ± 8.1
0.0168 ± 0.0018	-4.811 ± 0.027	0.689 ± 0.054	28.8 ± 4.5
0.0146 ± 0.0014	-21.794 ± 0.032	2.10 ± 0.12	268 ± 29
0.00535 ± 0.00026	-26.11 ± 0.82	5.3 ± 1.1	1697 ± 687
0.0528 ± 0.0020	-5.302 ± 0.072	2.276 ± 0.059	314 ± 16
0.00313 ± 0.00027	-15.30 ± 0.28	2.96 ± 0.38	530 ± 136
B0404+768 (WSRT); $N_{\text{comp}} = 8$ ; $\chi_r^2 = 0.988$ :			
0.00261 ± 0.00053	11.57 ± 0.26	1.54 ± 0.38	144 ± 70
0.06115 ± 0.00092	3.183 ± 0.029	1.566 ± 0.040	148.6 ± 7.5
0.2533 ± 0.0081	-0.4963 ± 0.0082	0.959 ± 0.017	55.8 ± 2.0
0.08553 ± 0.00097	-10.897 ± 0.017	1.328 ± 0.027	106.9 ± 4.3
0.04637 ± 0.00082	-13.606 ± 0.031	1.326 ± 0.040	106.6 ± 6.4
0.1497 ± 0.0076	-0.901 ± 0.035	1.934 ± 0.045	227 ± 10
0.0156 ± 0.0013	-6.490 ± 0.046	1.03 ± 0.11	64 ± 14
0.0307 ± 0.0014	-4.49 ± 0.17	8.82 ± 0.17	4718 ± 182
B0407-658 (ATCA); $N_{\text{comp}} = 7$ ; $\chi_r^2 = 0.981$ :			
0.1117 ± 0.0027	16.3923 ± 0.0089	1.047 ± 0.018	66.4 ± 2.3
0.00228 ± 0.00057	19.8 ± 1.4	8.4 ± 1.6	4285 ± 1576
0.02588 ± 0.00077	0.497 ± 0.029	1.304 ± 0.049	103.1 ± 7.6
0.00144 ± 0.00025	49.1 ± 1.1	7.8 ± 1.6	3667 ± 1460
0.00280 ± 0.00046	-0.52 ± 0.75	7.5 ± 1.2	3437 ± 1124
0.0417 ± 0.0026	17.053 ± 0.058	2.348 ± 0.076	334 ± 21
0.00265 ± 0.00057	-18.26 ± 0.27	1.52 ± 0.38	140 ± 69
B0518+165 (WSRT); $N_{\text{comp}} = 13$ ; $\chi_r^2 = 1.048$ :			
0.02574 ± 0.00076	-22.138 ± 0.021	1.039 ± 0.038	65.4 ± 4.9
0.01885 ± 0.00054	-21.585 ± 0.066	5.21 ± 0.12	1645 ± 79
0.00379 ± 0.00059	-12.89 ± 0.15	1.15 ± 0.23	80 ± 33
0.221 ± 0.021	-0.675 ± 0.030	0.945 ± 0.048	54.1 ± 5.6
0.0266 ± 0.0020	-6.12 ± 0.24	3.93 ± 0.20	936 ± 100
0.136 ± 0.013	-2.01 ± 0.12	1.242 ± 0.080	93 ± 12
0.2653 ± 0.0057	1.051 ± 0.027	1.151 ± 0.029	80.3 ± 4.2
0.0841 ± 0.0027	4.85 ± 0.34	6.41 ± 0.29	2491 ± 235
1.0378 ± 0.0073	5.968 ± 0.012	1.162 ± 0.011	81.8 ± 1.6
0.327 ± 0.017	7.354 ± 0.018	0.762 ± 0.024	35.2 ± 2.2
0.4060 ± 0.0042	8.965 ± 0.018	1.488 ± 0.019	134.2 ± 3.6
0.00102 ± 0.00033	21.91 ± 0.83	3.0 ± 1.3	532 ± 490
0.00107 ± 0.00042	28.13 ± 0.56	1.63 ± 0.81	160 ± 163
B0531+194 (GMRT); $N_{\text{comp}} = 11$ ; $\chi_r^2 = 1.123$ :			
0.0021 ± 0.0011	-10.3 ± 1.9	4.5 ± 1.7	1200 ± 972
0.0111 ± 0.0030	-2.43 ± 0.17	1.46 ± 0.27	129 ± 50
0.00199 ± 0.00051	-27.6 ± 1.8	3.4 ± 1.8	693 ± 767
0.0084 ± 0.0012	-23.13 ± 0.27	2.39 ± 0.25	345 ± 76
0.387 ± 0.014	1.4574 ± 0.0085	1.142 ± 0.018	79.0 ± 2.7
0.229 ± 0.020	2.55 ± 0.16	2.69 ± 0.17	440 ± 57
0.057 ± 0.017	4.29 ± 0.34	8.10 ± 0.81	3980 ± 841
0.151 ± 0.017	6.202 ± 0.054	1.62 ± 0.11	159 ± 22
0.2714 ± 0.0092	9.213 ± 0.016	1.537 ± 0.031	143.1 ± 6.2
0.0301 ± 0.0040	12.050 ± 0.099	1.38 ± 0.13	116 ± 23
0.00624 ± 0.00048	21.05 ± 0.13	2.06 ± 0.21	256 ± 55

**Table A1.** (continued) The parameters of the multi-Gaussian fits.

$\tau_{\text{peak}}$	$V_c$ km s <sup>-1</sup>	$b$ km s <sup>-1</sup>	$T_D$ K
B0538+498 (WSRT); $N_{\text{comp}} = 20$ ; $\chi_r^2 = 1.095$ :			
0.0645 ± 0.0024	4.720 ± 0.022	1.251 ± 0.023	94.9 ± 3.7
0.336 ± 0.010	0.79 ± 0.12	2.44 ± 0.10	360 ± 32
0.211 ± 0.016	-0.4550 ± 0.0094	1.087 ± 0.024	71.6 ± 3.3
0.0278 ± 0.0024	-1.94 ± 0.54	7.66 ± 0.37	3554 ± 359
0.084 ± 0.018	-2.32 ± 0.13	1.730 ± 0.083	181 ± 18
0.718 ± 0.080	-8.091 ± 0.042	0.869 ± 0.015	45.8 ± 1.6
0.210 ± 0.065	-8.92 ± 0.19	0.917 ± 0.086	51 ± 10
0.1561 ± 0.0059	-11.022 ± 0.010	0.989 ± 0.026	59.3 ± 3.3
0.1584 ± 0.0066	-11.267 ± 0.080	3.743 ± 0.061	849 ± 29
0.0449 ± 0.0028	-13.855 ± 0.030	1.089 ± 0.043	71.9 ± 5.9
0.01407 ± 0.00025	-19.664 ± 0.019	1.367 ± 0.031	113.3 ± 5.4
0.00232 ± 0.00013	-27.42 ± 0.43	5.89 ± 0.78	2103 ± 584
0.00236 ± 0.00030	-34.51 ± 0.13	1.58 ± 0.23	152 ± 47
0.00216 ± 0.00018	-41.16 ± 0.71	6.6 ± 1.4	2643 ± 1136
0.00273 ± 0.00028	-43.591 ± 0.087	1.21 ± 0.15	89 ± 24
0.00077 ± 0.00030	-49.44 ± 0.21	0.66 ± 0.32	27 ± 27
0.000644 ± 0.000095	-55.8 ± 1.5	6.7 ± 2.4	2693 ± 2004
0.000337 ± 0.000090	-73.0 ± 1.5	6.3 ± 2.3	2378 ± 1841
0.00065 ± 0.00012	-115.83 ± 0.51	3.29 ± 0.73	656 ± 306
0.00373 ± 0.00016	-124.236 ± 0.068	1.941 ± 0.097	228 ± 24
B0831+557 (WSRT); $N_{\text{comp}} = 7$ ; $\chi_r^2 = 1.000$ :			
0.00194 ± 0.00047	-5.59 ± 0.63	2.25 ± 0.84	308 ± 229
0.0596 ± 0.0065	3.355 ± 0.035	1.238 ± 0.063	92.9 ± 9.4
0.0289 ± 0.0072	0.959 ± 0.074	1.32 ± 0.13	105 ± 21
0.0321 ± 0.0094	1.94 ± 0.11	3.31 ± 0.31	664 ± 124
0.02651 ± 0.00056	-37.950 ± 0.023	1.329 ± 0.032	107.0 ± 5.2
0.00377 ± 0.00038	-56.20 ± 0.25	3.03 ± 0.35	557 ± 128
0.00375 ± 0.00055	-65.76 ± 0.16	1.35 ± 0.23	111 ± 38
B0834-196 (GMRT); $N_{\text{comp}} = 7$ ; $\chi_r^2 = 0.943$ :			
0.00124 ± 0.00044	50.73 ± 0.94	3.3 ± 1.3	643 ± 509
0.0120 ± 0.0014	11.07 ± 0.16	4.15 ± 0.38	1045 ± 186
0.0200 ± 0.0015	11.177 ± 0.042	1.197 ± 0.092	87 ± 13
0.0477 ± 0.0034	2.739 ± 0.022	0.784 ± 0.046	37.3 ± 4.2
0.0420 ± 0.0058	-0.721 ± 0.065	1.44 ± 0.11	126 ± 18
0.1414 ± 0.0045	2.308 ± 0.055	2.442 ± 0.071	362 ± 20
0.0081 ± 0.0023	-2.8 ± 1.8	3.8 ± 1.3	896 ± 583
B0906+430 (WSRT); $N_{\text{comp}} = 3$ ; $\chi_r^2 = 1.035$ :			
0.00262 ± 0.00030	12.47 ± 0.27	3.14 ± 0.45	598 ± 175
0.00355 ± 0.00050	1.97 ± 0.10	0.93 ± 0.16	52 ± 18
0.00113 ± 0.00017	3.1 ± 1.9	16.4 ± 2.0	16320 ± 4179
B1151-348 (GMRT); $N_{\text{comp}} = 10$ ; $\chi_r^2 = 1.083$ :			
0.00217 ± 0.00043	-35.66 ± 0.50	2.15 ± 0.72	279 ± 194
0.00438 ± 0.00044	-31.05 ± 0.24	2.02 ± 0.34	247 ± 86
0.00442 ± 0.00059	-18.62 ± 0.17	1.22 ± 0.24	90 ± 37
0.00658 ± 0.00052	-14.87 ± 0.26	1.88 ± 0.44	214 ± 104
0.00872 ± 0.00073	-11.28 ± 0.19	1.76 ± 0.31	187 ± 68
0.0880 ± 0.0027	-5.583 ± 0.015	1.274 ± 0.029	98.4 ± 4.7
0.0381 ± 0.0034	-4.198 ± 0.079	4.27 ± 0.17	1104 ± 91
0.0430 ± 0.0025	-2.425 ± 0.019	1.021 ± 0.047	63.2 ± 6.1
0.02396 ± 0.00057	6.605 ± 0.029	1.303 ± 0.043	102.9 ± 7.1
0.00531 ± 0.00053	10.08 ± 0.13	1.46 ± 0.20	129 ± 37

**Table A1.** (continued) The parameters of the multi-Gaussian fits.

$\tau_{\text{peak}}$	$V_c$ km s <sup>-1</sup>	$b$ km s <sup>-1</sup>	$T_D$ K
B1245–197 (GMRT); $N_{\text{comp}} = 6$ ; $\chi_r^2 = 1.006$ :			
0.00309 ± 0.00094	-17.11 ± 0.20	0.79 ± 0.28	38 ± 27
0.00296 ± 0.00095	-12.19 ± 0.22	0.82 ± 0.32	40 ± 32
0.00728 ± 0.00067	-6.80 ± 0.57	2.95 ± 0.69	529 ± 249
0.0243 ± 0.0081	-3.39 ± 0.11	1.45 ± 0.20	127 ± 36
0.0108 ± 0.0034	-1.2 ± 1.2	2.52 ± 0.84	385 ± 257
0.00373 ± 0.00084	9.15 ± 0.18	0.97 ± 0.25	57 ± 30
B1328+254 (WSRT); $N_{\text{comp}} = 4$ ; $\chi_r^2 = 1.027$ :			
0.00131 ± 0.00016	-23.47 ± 0.29	2.84 ± 0.44	490 ± 152
0.00132 ± 0.00015	-3.29 ± 0.28	3.04 ± 0.40	559 ± 149
0.00048 ± 0.00015	11.23 ± 0.74	2.8 ± 1.0	483 ± 361
0.00098 ± 0.00023	-17.95 ± 0.26	1.26 ± 0.37	96 ± 57
B1328+307 (WSRT); $N_{\text{comp}} = 4$ ; $\chi_r^2 = 1.025$ :			
0.00654 ± 0.00022	-7.371 ± 0.045	1.949 ± 0.085	230 ± 20
0.00730 ± 0.00024	-14.281 ± 0.029	1.122 ± 0.047	76.3 ± 6.5
0.00549 ± 0.00021	-28.785 ± 0.041	1.357 ± 0.059	112 ± 10
0.00109 ± 0.00019	-8.41 ± 0.68	9.2 ± 1.0	5143 ± 1168
B1345+125 (GMRT); $N_{\text{comp}} = 5$ ; $\chi_r^2 = 1.130$ :			
0.00298 ± 0.00085	-48.06 ± 0.14	0.59 ± 0.19	21 ± 15
0.0080 ± 0.0010	-3.930 ± 0.074	0.80 ± 0.12	38 ± 12
0.0799 ± 0.0011	-1.173 ± 0.011	1.454 ± 0.020	128.2 ± 3.7
0.00876 ± 0.00099	-3.08 ± 0.22	5.28 ± 0.32	1691 ± 220
0.00180 ± 0.00053	19.52 ± 0.37	1.52 ± 0.52	140 ± 101
B1611+343 (WSRT); $N_{\text{comp}} = 2$ ; $\chi_r^2 = 1.014$ :			
0.00177 ± 0.00021	-4.10 ± 0.40	4.14 ± 0.56	1037 ± 278
0.00093 ± 0.00025	-30.32 ± 0.56	2.54 ± 0.80	390 ± 244
B1641+399 (WSRT); $N_{\text{comp}} = 1$ ; $\chi_r^2 = 1.003$ :			
0.00082 ± 0.00013	-1.25 ± 0.61	4.72 ± 0.86	1350 ± 492
B1814–637 (ATCA); $N_{\text{comp}} = 3$ ; $\chi_r^2 = 1.027$ :			
0.3083 ± 0.0051	-0.9024 ± 0.0035	0.8638 ± 0.0095	45.2 ± 1.0
0.1088 ± 0.0049	-1.055 ± 0.017	2.052 ± 0.051	255 ± 13
0.00927 ± 0.00092	-2.37 ± 0.25	7.53 ± 0.42	3433 ± 388
B1827–360 (GMRT); $N_{\text{comp}} = 9$ ; $\chi_r^2 = 1.097$ :			
0.00152 ± 0.00048	-15.29 ± 0.32	1.27 ± 0.49	97 ± 78
0.00266 ± 0.00080	-6.1 ± 2.9	5.3 ± 2.6	1678 ± 1731
0.0057 ± 0.0019	-3.86 ± 0.27	0.98 ± 0.28	59 ± 35
0.0349 ± 0.0017	-1.944 ± 0.057	1.329 ± 0.088	107 ± 15
0.1371 ± 0.0054	4.395 ± 0.098	1.71 ± 0.11	177 ± 23
0.0640 ± 0.0061	4.44 ± 0.27	5.29 ± 0.24	1699 ± 165
0.0231 ± 0.0076	4.017 ± 0.042	0.73 ± 0.11	32 ± 11
0.1023 ± 0.0086	6.865 ± 0.090	1.596 ± 0.078	154 ± 16
0.0439 ± 0.0013	10.961 ± 0.019	1.076 ± 0.032	70.2 ± 4.3

**Table A1.** (continued) The parameters of the multi-Gaussian fits.

$\tau_{\text{peak}}$	$V_c$ km s <sup>-1</sup>	$b$ km s <sup>-1</sup>	$T_D$ K
B1921–293 (GMRT); $N_{\text{comp}} = 7$ ; $\chi_r^2 = 0.995$ :			
0.191 ± 0.015	4.736 ± 0.016	1.012 ± 0.030	62.1 ± 3.7
0.0640 ± 0.0083	3.163 ± 0.030	0.736 ± 0.048	32.8 ± 4.2
0.0240 ± 0.0028	4.43 ± 0.26	6.16 ± 0.39	2301 ± 294
0.170 ± 0.015	4.171 ± 0.025	2.202 ± 0.086	294 ± 23
0.00800 ± 0.00098	13.31 ± 0.36	3.49 ± 0.40	739 ± 170
0.00279 ± 0.00053	-13.96 ± 0.30	1.89 ± 0.42	218 ± 96
0.00164 ± 0.00020	42.4 ± 1.3	13.2 ± 1.9	10605 ± 3046
B2050+364 (WSRT); $N_{\text{comp}} = 17$ ; $\chi_r^2 = 0.902$ :			
0.00085 ± 0.00025	-76.6 ± 2.8	10.2 ± 4.3	6246 ± 5027
0.00085 ± 0.00029	-39.7 ± 2.2	7.6 ± 3.5	3469 ± 3041
0.00168 ± 0.00047	-52.79 ± 0.68	2.85 ± 0.99	492 ± 325
0.00224 ± 0.00064	30.31 ± 0.35	1.48 ± 0.52	133 ± 88
0.00689 ± 0.00062	-64.59 ± 0.13	1.85 ± 0.21	208 ± 44
0.00742 ± 0.00054	-21.73 ± 0.14	2.33 ± 0.20	329 ± 53
0.01135 ± 0.00089	-12.214 ± 0.088	1.53 ± 0.16	142 ± 28
0.0164 ± 0.0014	-6.931 ± 0.051	0.788 ± 0.084	37.6 ± 7.6
0.0973 ± 0.0026	-1.600 ± 0.023	1.637 ± 0.044	162.5 ± 8.4
0.0438 ± 0.0036	1.625 ± 0.048	1.299 ± 0.097	102 ± 15
0.1559 ± 0.0043	8.202 ± 0.012	0.901 ± 0.025	49.2 ± 2.6
0.188 ± 0.034	9.14 ± 0.25	3.55 ± 0.30	764 ± 122
0.0428 ± 0.0067	14.17 ± 0.14	1.16 ± 0.17	81 ± 23
0.0532 ± 0.0064	15.823 ± 0.089	0.961 ± 0.080	56.0 ± 8.8
0.032 ± 0.022	14.5 ± 3.9	5.3 ± 2.0	1727 ± 1254
0.00731 ± 0.00069	25.24 ± 0.17	1.97 ± 0.26	236 ± 58
0.0414 ± 0.0031	-0.46 ± 0.62	7.59 ± 0.52	3488 ± 451
B2200+364 (WSRT); $N_{\text{comp}} = 11$ ; $\chi_r^2 = 0.952$ :			
0.00181 ± 0.00056	-29.3 ± 2.3	7.7 ± 3.6	3632 ± 3267
0.0051 ± 0.0018	-17.68 ± 0.24	0.83 ± 0.35	42 ± 34
0.0041 ± 0.0011	-10.30 ± 0.53	2.42 ± 0.77	355 ± 221
0.0182 ± 0.0016	-20.592 ± 0.080	1.22 ± 0.13	90 ± 19
0.192 ± 0.020	-1.622 ± 0.022	0.557 ± 0.043	18.8 ± 2.8
0.289 ± 0.020	-0.918 ± 0.094	1.449 ± 0.084	127 ± 14
0.218 ± 0.012	1.041 ± 0.097	4.18 ± 0.12	1058 ± 60
0.315 ± 0.014	1.354 ± 0.037	0.981 ± 0.040	58.4 ± 4.6
0.0757 ± 0.0043	6.428 ± 0.035	1.216 ± 0.072	90 ± 10
0.0228 ± 0.0013	13.808 ± 0.069	1.439 ± 0.098	126 ± 17
0.1031 ± 0.0017	18.149 ± 0.012	0.874 ± 0.017	46.3 ± 1.7
B2203–188 (WSRT); $N_{\text{comp}} = 6$ ; $\chi_r^2 = 0.996$ :			
0.06515 ± 0.00062	7.802 ± 0.010	1.053 ± 0.018	67.3 ± 2.3
0.02882 ± 0.00054	4.948 ± 0.027	1.437 ± 0.043	125.2 ± 7.5
0.00119 ± 0.00034	-21.91 ± 0.76	3.6 ± 1.3	796 ± 563
0.00140 ± 0.00018	-3.6 ± 2.1	15.5 ± 2.8	14617 ± 5183
0.00377 ± 0.00063	10.23 ± 0.15	0.93 ± 0.23	52 ± 25
0.00324 ± 0.00096	-6.138 ± 0.092	0.39 ± 0.13	9.0 ± 6.2
B2223–052 (GMRT); $N_{\text{comp}} = 7$ ; $\chi_r^2 = 1.034$ :			
0.0976 ± 0.0025	-6.919 ± 0.013	1.662 ± 0.025	167.5 ± 5.0
0.0419 ± 0.0031	-4.41 ± 0.13	4.81 ± 0.18	1405 ± 105
0.1039 ± 0.0024	-3.943 ± 0.010	1.236 ± 0.019	92.6 ± 2.9
0.0085 ± 0.0012	2.34 ± 0.14	1.330 ± 0.212	107 ± 35
0.0232 ± 0.0024	5.93 ± 0.24	2.23 ± 0.16	302 ± 44
0.0232 ± 0.0036	7.238 ± 0.046	1.059 ± 0.097	68 ± 13
0.00210 ± 0.00044	11.27 ± 0.40	1.57 ± 0.57	149 ± 110